AGU PUBLICATIONS

JGR

Journal of Geophysical Research: Planets

RESEARCH ARTICLE
10.1002/2014JE004713

Key Points:
- We analyze Mercury's gravity and topography data returned by MESSENGER
- Mercury's topography is compensated by both shallow and deep mechanisms
- We invert the observed data to map crustal thickness and deep mass anomalies

Correspondence to:
P. B. James,
peterj@ldeo.columbia.edu

Citation:
James, P. B., M. T. Zuber, R. J. Phillips, and S. C. Solomon (2015), Support of long-wavelength topography on Mercury inferred from MESSENGER measurements of gravity and topography, *J. Geophys. Res. Planets*, *120*, 287–310, doi:10.1002/2014JE004713.

Received 7 AUG 2014
Accepted 20 DEC 2014
Accepted article online 29 DEC 2014
Published online 26 FEB 2015

Support of long-wavelength topography on Mercury inferred from MESSENGER measurements of gravity and topography

Peter B. James[1], Maria T. Zuber[2], Roger J. Phillips[3], and Sean C. Solomon[1,4]

[1]Lamont-Doherty Earth Observatory, Columbia University, Palisades, New York, USA, [2]Department of Earth, Atmospheric and Planetary Sciences, Massachusetts Institute of Technology, Cambridge, Massachusetts, USA, [3]Planetary Science Directorate, Southwest Research Institute, Boulder, Colorado, USA, [4]Department of Terrestrial Magnetism, Carnegie Institution of Washington, Washington, District of Columbia, USA

Abstract To explore the mechanisms of support of surface topography on Mercury, we have determined the admittances and correlations of topography and gravity in Mercury's northern hemisphere from measurements obtained by NASA's MErcury Surface, Space ENvironment, GEochemistry, and Ranging (MESSENGER) spacecraft. These admittances and correlations can be interpreted in the context of a number of theoretical scenarios, including flexural loading and dynamic flow. We find that long-wavelength (spherical harmonic degree $l < 15$) surface topography on Mercury is primarily supported through a combination of crustal thickness variations and deep mass anomalies. The deep mass anomalies may be interpreted either as lateral variations in mantle density or as relief on compositional interfaces. Domical topographic swells are associated with high admittances and are compensated at 300–400 km depth in the lower reaches of Mercury's mantle. Quasi-linear topographic rises are primarily associated with shallow crustal compensation and are weakly correlated with positive mass anomalies in the mantle. The center of the Caloris basin features some of the thinnest crust on the planet, and the basin is underlain by a large negative mass anomaly. We also explore models of dynamic flow in the presence of compositional stratification above the liquid core. If there is substantial compositional stratification in Mercury's solid outer shell, relaxation of perturbed compositional interfaces may be capable of creating and sustaining long-wavelength topography.

1. Introduction

The gravity field and topography of Mercury measured by NASA's MErcury Surface, Space ENvironment, GEochemistry, and Ranging (MESSENGER) spacecraft [*Santo et al.*, 2001; *Leary et al.*, 2007; *McAdams et al.*, 2007] collectively provide a powerful tool for investigating the interior structure and evolution of the innermost planet. Mercury's gravity field is a function of the density distribution inside the planet and the surface topography, and although inversion of a gravity field is nonunique (i.e., a variety of internal mass distributions can produce the same gravity field), we can characterize Mercury's interior with appropriate simplifying assumptions. The gravity and topography associated with multiple isostatic, dynamic, and flexural compensation scenarios can be quantified [*Wieczorek*, 2007], and a comparison of spherical harmonic expansions of observed gravity and topography with the predictions of such scenarios offers the opportunity to improve our knowledge of the structure and evolution of Mercury's crust and mantle.

The estimation of admittances and correlations from spherical harmonic representations of gravity and topography has been successfully applied to studies of Earth [*Forsyth*, 1985; *Watts*, 2001; *McKenzie*, 2003], the Moon [*Wieczorek and Phillips*, 1997; *Wieczorek et al.*, 2013], Venus [*McKenzie*, 1994; *Simons et al.*, 1997; *James et al.*, 2013], and Mars [*McGovern et al.*, 2002; *Wieczorek and Zuber*, 2004; *Belleguic et al.*, 2005]. In this paper we perform the first such spectral analysis of gravity and topography on Mercury, although MESSENGER's eccentric orbit and high northern periapsis latitude restrict our analysis to the planet's northern hemisphere. The results of our spectral analysis motivate a dual inversion of gravity and topography in which we solve for crustal thickness and mantle dynamic flow. Finally, we perform viscous flow calculations for a compositionally stratified interior, and from that analysis and with additional constraints from Mercury's geology and surface chemistry, we describe the implications of our work for Mercury's structure and evolution.

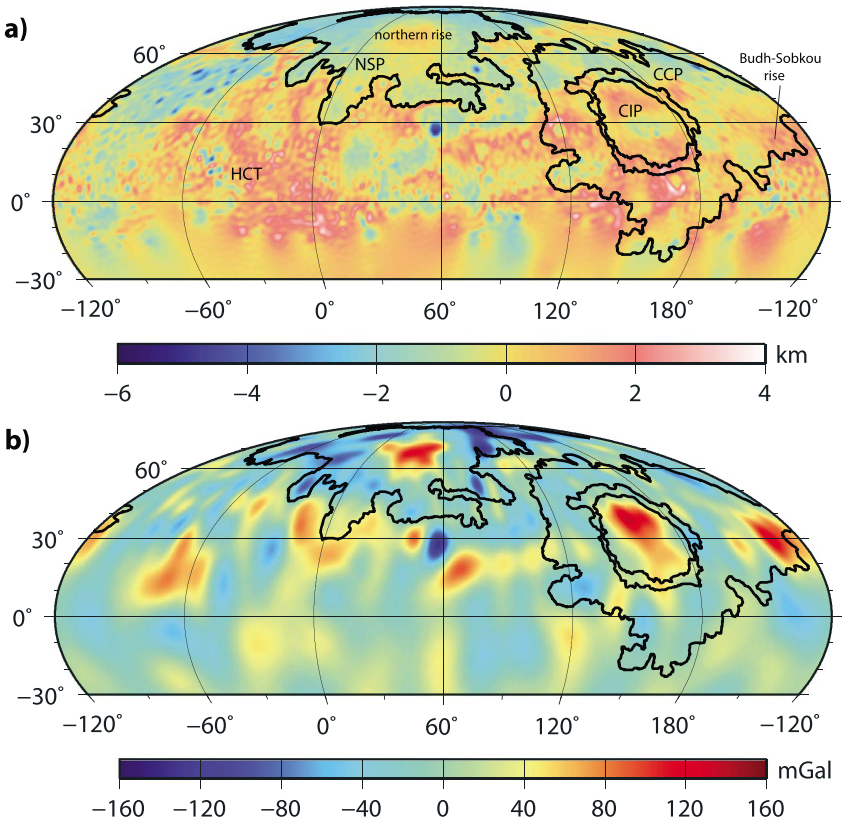

Figure 1. (a) Topography and (b) free-air gravity anomaly fields of Mercury determined by MESSENGER: equal-area Mollweide projections. Labeled regions include heavily cratered terrain (HCT), northern smooth plains (NSP), the northern rise, the Budh-Sobkou rise, Caloris interior plains (CIP), and circum-Caloris plains (CCP).

2. Topography and Gravity

The Mercury Laser Altimeter (MLA) [*Cavanaugh et al.*, 2007] on the MESSENGER spacecraft has been collecting orbital measurements of Mercury's shape since March 2011. We denote shape, i.e., the planetary radius from the center of mass as a function of colatitude (θ) and longitude (ϕ), by $H(\Omega)$, where $\Omega \in (\theta, \phi)$ represents position on the surface of a sphere (Figure 1a). MLA shape measurements are absent in much of the southern hemisphere as a consequence of MESSENGER's highly eccentric orbit. Individual measurements of radius made by MLA have precisions of <1 m, and uncertainties with respect to Mercury's center of mass are less than ±25 m [*Zuber et al.*, 2012].

In conjunction with images from MESSENGER's Mercury Dual Imaging System [*Hawkins et al.*, 2007], MLA topography has helped to characterize and distinguish geological provinces [*Zuber et al.*, 2012]. Among the most distinctive physiographic features on Mercury's surface is the Caloris basin, the youngest and best preserved large impact basin on the planet [*Spudis and Guest*, 1988; *Head et al.*, 2007; *Murchie et al.*, 2008]. The interior of the basin has been resurfaced with volcanic smooth plains, the Caloris interior plains (CIP), which were first observed in their entirety in images acquired during MESSENGER's flybys of Mercury prior to orbit insertion [*Murchie et al.*, 2008]. MLA observations confirmed the presence of long-wavelength topographic undulations in parts of the CIP [*Zuber et al.*, 2012] first seen in stereo-derived topography [*Oberst et al.*, 2010]. These undulations have raised portions of the basin interior to elevations above the basin rim crest.

The Caloris basin is also surrounded by extensive smooth plains, the circum-Caloris plains (CCP). Parts of the CCP are associated with the hummocky Odin Formation [*Fassett et al.*, 2009; *Denevi et al.*, 2013], which, on the basis of color and morphology, has been interpreted as Caloris basin impact ejecta. Size-frequency distributions of impact craters, however, indicate that the CCP are younger than the Caloris impact event and therefore must be primarily volcanic in origin [*Fassett et al.*, 2009].

The other major area of smooth plains on Mercury is the northern smooth plains (NSP) unit. The NSP unit mostly occupies low-lying terrain, but within the plains is a broad domical topographic swell, centered at 68°N, 32°E, approximately 1000 km across, and displaying 1.5 km in relief, informally known as the "northern rise." The northern rise is not associated with substantially thickened crust [*Smith et al.*, 2012]. MLA profiles reveal that the floors of volcanically buried craters on the flanks of the northern rise are tilted in directions and by amounts that approximately match those of the regional topographic slope, indicating that the surface of the northern rise was uplifted at some point after the emplacement of the NSP [*Klimczak et al.*, 2012; *Zuber et al.*, 2012].

The remainder of Mercury's surface is largely characterized by heavily cratered terrain and intercrater plains (here grouped together and denoted by "HCT") and is generally older than the volcanic smooth plains [*Spudis and Guest*, 1988]. Long-wavelength topography in the HCT is dominated by a number of quasi-linear rises that are associated with thickened crust and are bordered in places by fold and thrust belts [*Zuber et al.*, 2012; *Byrne et al.*, 2014]. However, at least one rise on the periphery of the HCT, the Budh-Sobkou rise at 30°N, 230°E, has a more circular shape, similar to that of the northern rise.

Radio tracking of the MESSENGER spacecraft [*Srinivasan et al.*, 2007] is providing information on the gravitational potential of Mercury [*Smith et al.*, 2012], from which the free-air gravity anomaly $g(\Omega)$ may be calculated (Figure 1b). In terms of resolution sufficient for spectral analysis of gravity, these data are mostly limited to the northern hemisphere because of MESSENGER's eccentric orbit. The HgM005 gravity field of Mercury [*Mazarico et al.*, 2014] includes spherical harmonic coefficients to degree and order 50 (resolving spatial blocks ~150 km across), but the power of the error surpasses the signal power for degrees above $l = 40$ and the resolution of the gravity field is even less than this figure when the full covariance matrix of the gravity field is taken into consideration. A map of the HgM005 gravity degree strength (i.e., the degree at which the uncertainty exceeds the signal for a given latitude and longitude) [*Mazarico et al.*, 2014, Figure 8b] shows that the resolution of the gravity field decreases from north to south with a maximum degree strength of $l > 36$ near the north pole, a minimum degree strength of $l < 10$ near the south pole, and degree strengths of approximately $l = 15$ at locations near the equator. The Caloris basin is associated with degree strengths in the range $l = 18$–28, and in the northern rise area, the degree strengths are $l = 30$–34. The harmonic expansion of Mercury's shape as measured by MLA [*Smith*, 2014] is known at a much greater resolution than is the gravity field in the northern hemisphere, and we ignore the shape uncertainty when modeling both the topography and the gravity field north of 30°S. We neglect the degree-1 coefficients of the topography (which give the offset between the centers of mass and figure) and the degree-2 coefficients of both the gravity and topography fields, given the uncertain influence of Mercury's history of despinning and orbital eccentricity on the variations of surface temperature with latitude and longitude.

Because comparisons of gravity and topography on Mercury are predominantly limited by the precision of the gravity field, it is imperative to quantify thoroughly the formal uncertainties in the HgM005 gravity field from its associated covariance matrix (see Appendix A). We performed eigenvalue decomposition on the full gravity covariance matrix, and we used the first 100 eigenvectors to produce many random realizations of error (termed "clone fields" by *Smith et al.* [2012]) under the assumption that there is no error in topography. These clone fields were applied to the nominal gravity data and localized with Slepian tapers (see section 4) in order to find the resulting distribution of admittances. We multiplied the nominal errors by a factor of 10 to ensure that we did not underestimate the true error, as recommended by *Mazarico et al.* [2014].

3. Constraints on Mercury's Interior Structure

Flyby encounters of Mercury by the Mariner 10 spacecraft confirmed the planet's high bulk density [*Anderson et al.*, 1987], which indicates the presence of a large metallic core [*Solomon*, 1976]. Mercury's distance from Earth and proximity to the Sun limit the effectiveness of Earth-based observations, but radar measurements successfully determined Mercury's obliquity (2.04 ± 0.08 arc min) and the amplitude (38.5 ± 1.6 arc sec) of the forced physical libration in longitude driven by solar gravitational torques [*Margot et al.*, 2007, 2012]. The second-degree zonal and sectorial coefficients, C_{20} and C_{22}, in the spherical harmonic expansion of the gravity field recovered by MESSENGER complemented the earlier obliquity and libration data to yield Mercury's polar moment of inertia and the fraction thereof contributed by Mercury's solid outer shell. These moment of inertia values constrain the depth to the top of Mercury's liquid core to about 400 km [*Smith et al.*, 2012].

A surficial sulfur abundance 10 times higher than that of Earth or the Moon and relatively low surface Fe abundances indicate that Mercury likely formed in a highly reducing environment [*Nittler et al.*, 2011], which may have allowed for partitioning of Si as well as S into Mercury's core [*Malavergne et al.*, 2010]. In a core of Fe-S-Si composition, a solid FeS layer could have formed at the top of the core for some thermal history models. Orbital parameters are consistent with but do not require the presence of such a high-density, solid FeS layer at the base of the mantle [*Hauck et al.*, 2013]. With or without this layer, the silicate portion of Mercury is thinner than was thought prior to MESSENGER observations [cf. *Smith et al.*, 2012].

Mercury's surface displays pervasive volcanic deposits, particularly in the northern hemisphere [*Denevi et al.*, 2013]. Evidence of flood volcanism, eroded flow channels, and a dearth of volcanic edifices point to low magma viscosities [*Head et al.*, 2011: *Byrne et al.*, 2013], which likely result from high degrees of partial melting and high lava eruption temperatures. Major element abundances inferred from MESSENGER's X-Ray Spectrometer [*Nittler et al.*, 2011; *Weider et al.*, 2012] and Gamma-Ray Spectrometer [*Peplowski et al.*, 2012; *Evans et al.*, 2012] are intermediate between low-Fe basaltic and komatiitic compositions [*Nittler et al.*, 2011; *Charlier et al.*, 2013]. Such compositions are broadly comparable to that of a high-degree melt of enstatite chondrite material, although the low-Fe abundance on Mercury is still higher than that of enstatite chondrite melts [*Weider et al.*, 2012; *Stockstill-Cahill et al.*, 2012]. Mercury's surface as a whole has lower Al and Ca concentrations than are observed on the surface of the Moon. Mercury thus shows no evidence for a lunar-like feldspar-rich crust produced during magma ocean differentiation, but the planet likely experienced multiple stages of interior melting following metal-silicate differentiation [*Brown and Elkins-Tanton*, 2009; *Charlier et al.*, 2013].

Mercury's HCT generally has higher Mg/Si, S/Si, and Ca/Si and lower Al/Si than the younger volcanic plains [*Weider et al.*, 2012]. The CIP and the NSP have similar elemental abundances, but the CCP are more similar to the HCT than to the smooth volcanic plains [*Weider et al.*, 2012]. The CIP and NSP likely crystalized from magmas derived from a mantle source that was more evolved than the source of the HCT, consistent with the relative ages of these terrains [*Weider et al.*, 2012]. However, the mantle from which melts were derived cannot have been globally homogeneous and likely included at least two different compositional groups [*Charlier et al.*, 2013].

4. Localized Spectra in Mercury's Northern Hemisphere

4.1. Admittance and Correlation

The ratios and correlations of gravity and topography can be used to distinguish between different mechanisms for supporting surface topography, such as crustal thickness variations, mantle dynamic flow, or lithospheric elastic stresses [e.g., *Forsyth*, 1985; *Richards and Hager*, 1984; *McGovern et al.*, 2002]. We elected to calculate spectra in the spherical harmonic domain rather than rely on scalar quantities because these compensation mechanisms often predominate at different wavelengths. Spectral analyses on a sphere take advantage of the fact that arbitrary real functions may be expressed as linear combinations of basis functions. For example, Mercury's shape $H(\Omega)$ may be expressed as a sum of spherical harmonic functions respectively weighted by the coefficients H_{lm}, called the "spherical harmonic coefficients" of H, where l and m are the spherical harmonic degree and order, respectively (see Appendix B for further explanation of the notation). The free-air gravity anomaly $g(\Omega)$ can be similarly decomposed into its spherical harmonic coefficients g_{lm}. The wavelength-dependent ratio of gravity to topography, Z_l, called the "admittance spectrum," may be calculated from the respective power spectra and cross-power spectrum of gravity and topography. The correlation of gravity and topography, γ_l (not to be confused with "coherence," which is the correlation squared), may similarly be calculated [*Wieczorek*, 2007].

4.2. Slepian Tapers

Because Mercury's upper crust may be divided into multiple geologically distinct terrains, it is useful to study the spatial variation of gravity/topography ratios and correlations in addition to the wavelength dependence of these quantities. Furthermore, data gaps in the southern hemisphere make spatial localization a necessity on Mercury. Methods that produce spectra for localized regions are called "spatio-spectral analyses."
A common spatio-spectral analysis involves creating a data taper, which may be applied as a movable filter to the global gravity or topography. In any spatio-spectral analysis, the power of the tapered data at a

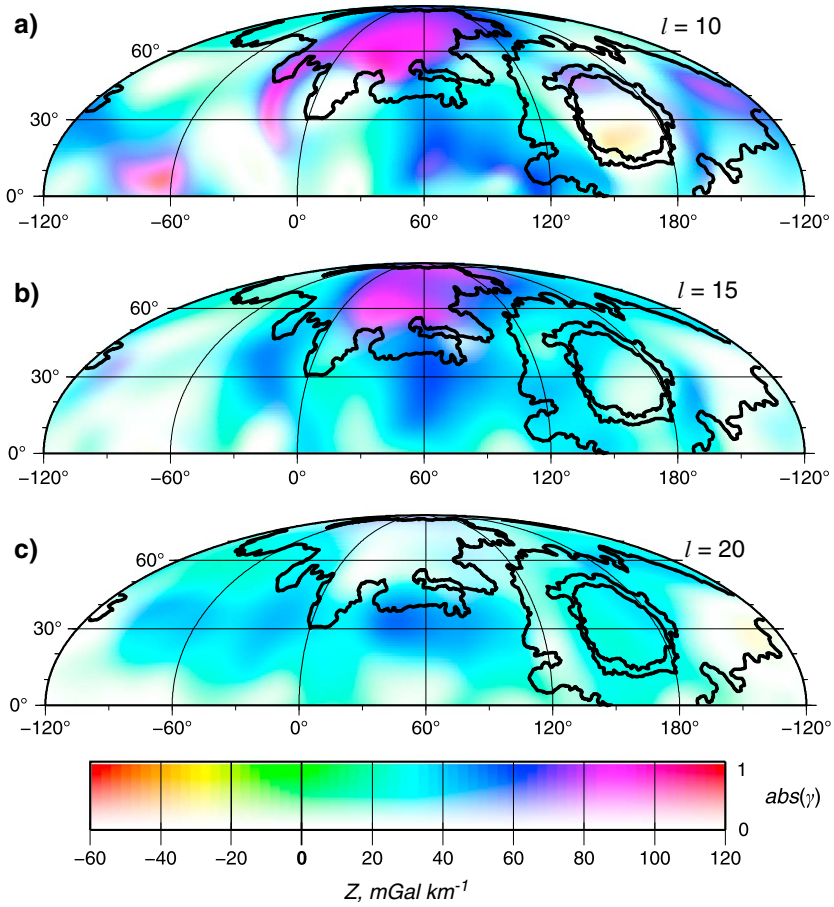

Figure 2. Single-taper admittance and coherence values for spherical harmonic degrees 10, 15, and 20. The hue denotes the localized admittance, and the shading represents the correlation of gravity and topography (see color bar).

particular wavelength will be contaminated by data at other wavelengths through a phenomenon known as "spectral leakage" [*Dahlen and Simons*, 2008]. Ideal localization may be accomplished using Slepian tapers, which maximize the concentration of a spherical function's energy (i.e., the function's squared amplitude) within a region while restricting spectral leakage. In practice, Slepian tapers are constructed with a combination of spherical harmonic functions that are evaluated in the spatial domain and multiplied by the global gravity and topography to produce the tapered gravity and topography. The tapered data may then be expanded into the spherical harmonic domain with equation (A2) and used to calculate an admittance spectrum (equation (A6)) and a correlation spectrum (equation (A7)). The highest degree and order of the Slepian taper is called the "bandwidth," and spectral leakage at a given degree is restricted to a range of degrees equal to plus or minus the bandwidth. It is important to note that even the ideal localization provided by Slepian tapers cannot remove the tradeoff between spatial localization and spectral fidelity.

In order to obtain an initial sense of the spatial variation in admittance and coherence on Mercury, we first applied a single zonal taper to the topography and gravity field over a grid in latitude and longitude. The tradeoff between spatial localization and spectral fidelity depends on the chosen taper bandwidth: a larger bandwidth allows for a more narrowly windowed data taper, but a smaller bandwidth reduces spectral leakage. For our analyses we selected tapers with a bandwidth of harmonic degree 8, since such a choice allows us to study the topographic swells that correspond approximately to harmonic degree 10. The resulting localization is imperfect; the first zonal taper for a polar cap concentrates 41% of the total energy within 10° of the center and 90% of the energy within 20° of the center. The localized admittance and correlation values are shown in Figure 2 for spherical harmonic degrees 10, 15, and 20. The two most prominent regions of high admittance appear to coincide with domical topographic rises: the northern rise

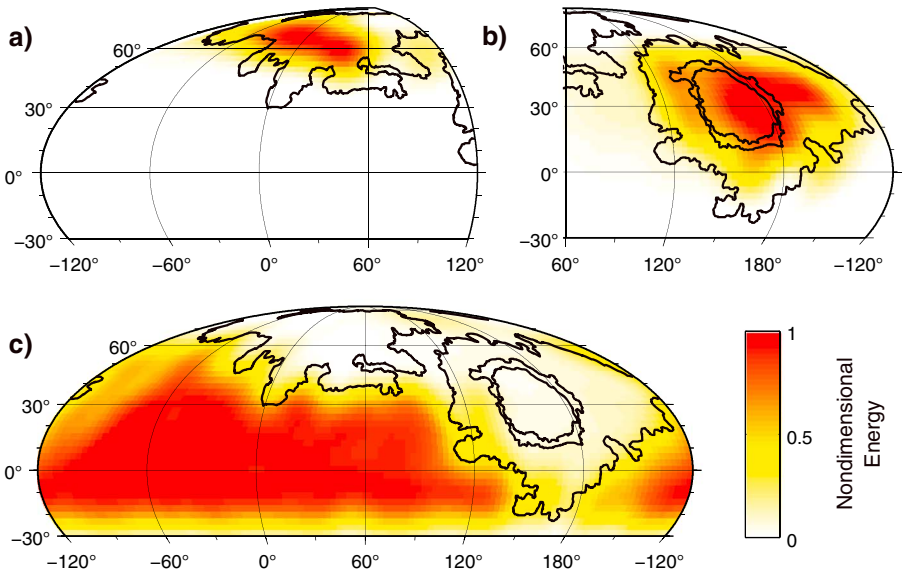

Figure 3. Normalized taper energy for (a) the northern smooth plains, (b) the Caloris plains (defined as the aggregate of the CIP and the CCP), and (c) heavily cratered terrain.

(centered at 68°N, 32°E) and the Budh-Sobkou rise (30°N, 230°E). Admittances in excess of 60 mGal km^{-1} are also observed near the topographic rise at the northernmost extent of the Caloris basin interior (40°N, 160°E), albeit with poor correlation. Large sections of the Caloris basin are characterized by poor correlations of gravity and topography and/or negative admittances, which are not uncommon in regions where multiple mechanisms of topographic compensation are superimposed.

4.3. Arbitrarily Shaped Regions

We next performed multitaper analysis of gravity and topography to complement the single-taper survey. The use of multiple orthogonal tapers results in a more thorough coverage of an arbitrarily shaped region, and the independent estimates of admittance and correlation provided by the various tapers make it straightforward to quantify uncertainty. Following the formalism of *Dahlen and Simons* [2008], a series of orthogonal Slepian tapers can be calculated so as to maximize energy within a desired region. We partitioned the northern hemisphere of Mercury into three physiographic regions: the NSP, the aggregate of the CIP and the CCP (collectively called the "Caloris plains"), and the HCT, which we defined simply as the remaining area north of 30°S. We retained only those tapers that localize >80% of their energy within each region, respectively. In Figure 3 we plot the normalized taper energy for each region. For a taper bandwidth of harmonic degree 8, there are two tapers well localized to the NSP, seven tapers well localized to the Caloris plains, and 32 tapers well localized to the HCT. Since the NSP and Caloris plains are not very large relative to the size of the degree-8 tapers, the chosen tapers do not perfectly follow the boundaries of the provinces, and the Caloris plains tapers sample the basin rim that separates the CIP from the CCP. In each region the spatio-spectral taper is most sensitive to data at the center of the region, and consequently, our analysis of Caloris is more sensitive to the CIP than it is to the CCP. For similar reasons, the tapers covering the NSP are relatively insensitive to the extremities of the plains.

4.4. Quantification of Uncertainty

We have calculated uncertainties in admittance spectra as a combination of measurement error and variance among tapered admittances. We produced noisy realizations of the admittance with the HgM005 gravity covariance matrix [*Mazarico et al.*, 2014], and the variance of these noisy spectra gives us the associated admittance uncertainty (see Appendix A). The other source of uncertainty arises from the fact that we have only a single realization of gravity and topography in a given region. *Wieczorek and Phillips* [1997] show that gravity/topography ratios in the spatial domain can be interpreted as a sum of spectrally weighted admittances, and tapered admittance estimates are similarly a convolution of admittances within the

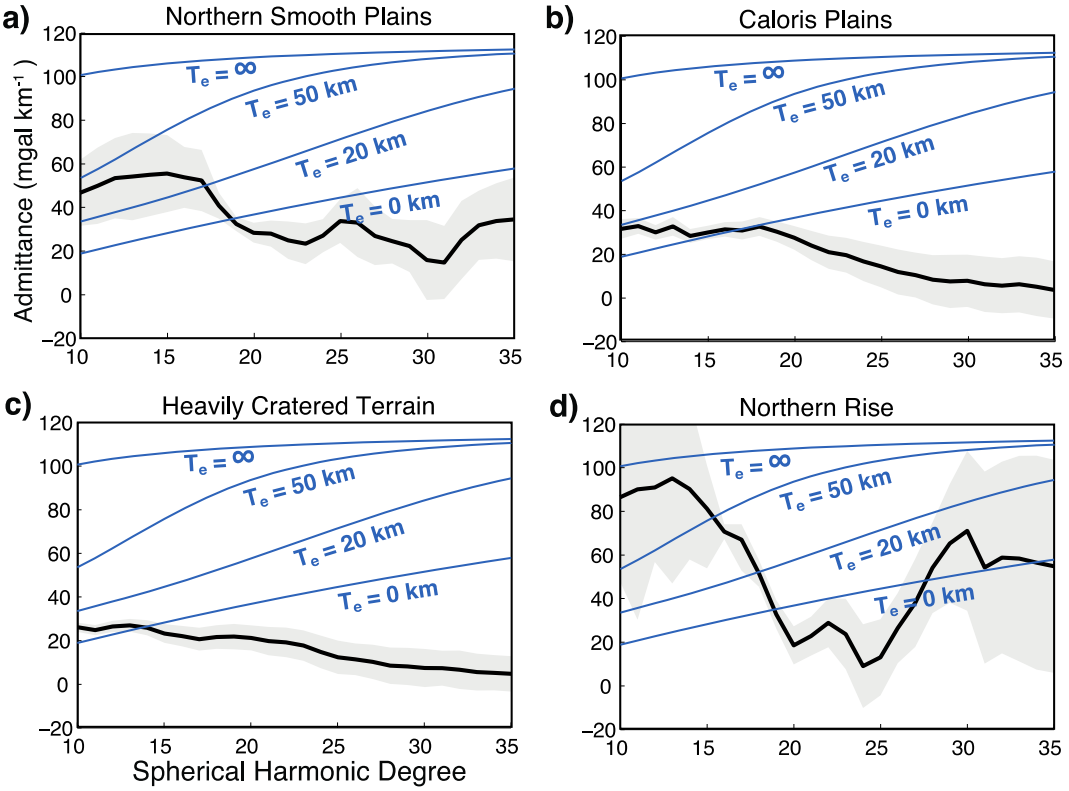

Figure 4. Observed admittance values (black) with error ranges (gray shading) for (a) the northern smooth plains, (b) the Caloris plains, (c) heavily cratered terrain, and (d) the northern rise. Theoretical admittance values are plotted for Airy compensation at the indicated compensation depth *D* (blue).

bandwidth of the taper as a result of spectral leakage. Because theoretical admittances typically vary with spherical harmonic degree, the observed admittance spectrum is dependent on the shape amplitude at different length scales, and any data taper will variably sample a function at different spherical harmonic degrees. Orthogonal Slepian tapers offer nearly independent estimates of gravity and topography spectra within a desired region, so the tapered variance can be estimated from the variance among tapers divided by the total number of tapers [*Wieczorek and Simons*, 2007]. Quantifying the effect of this variance for a single taper is more laborious; we estimated single-taper variance by generating many synthetic topography fields with power spectra that match Mercury's topography power spectrum. We then created synthetic gravity fields by multiplying topography by a range of admittance spectra proportional to $l^{-0.5}$, the approximate spectral slope of the global admittance spectrum between spherical harmonic degrees 5 and 20. We applied single Slepian tapers to the north poles of these synthetic topography and gravity fields and calculated the resulting admittances. We then determined the range of admittances that could produce the observed localized admittance within a confidence interval.

Admittances for the NSP, the Caloris plains, the HCT, and the northern rise are plotted in Figures 4–6 along with their uncertainties. Note that the small admittance errors associated with the HCT result from the broad areal expanse of the associated data taper rather than high data quality within the region. Model admittance curves from the theory in Appendix C are shown for comparison. In Figure 4 admittance spectra are plotted for several apparent depths of compensation for an Airy compensation model. Figure 5 shows admittances for lithospheric flexure in response to top loading for a variety of values of the effective elastic thickness of the lithosphere, T_e, and Figure 6 shows admittances for lithospheric flexure in response to bottom loading. None of these models fit a single compensation mechanism well at all wavelengths, but the lower degrees ($l < 15$) have relatively high admittances, which correspond to either greater compensation depths or larger values of T_e. Correlations of gravity and topography (Figure 7) are significantly less than unity almost everywhere on the planet, although the northern rise at low degrees is a notable exception. The

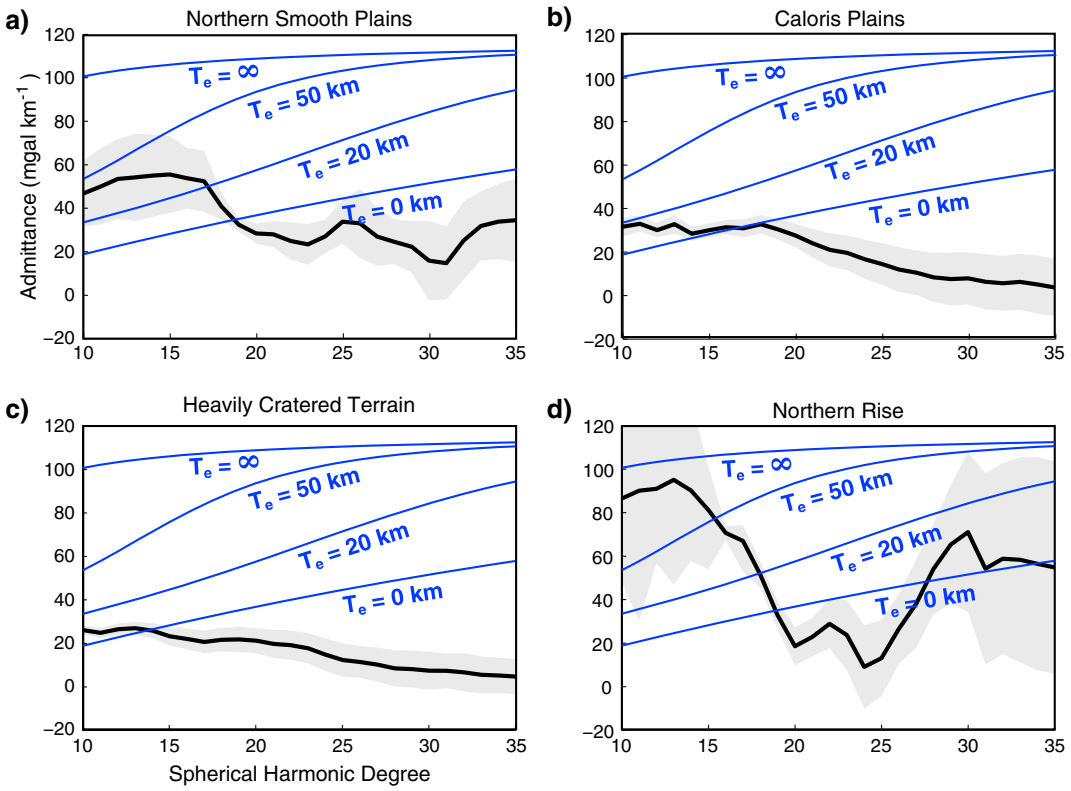

Figure 5. Observed admittance values (black) with error ranges (gray shading) and theoretical admittance values for top-loaded elastic shells having the indicated values of shell thickness T_e (blue).

presence of noise in gravity and topography data will typically move the observed gravity/topography correlation closer to zero, but gravity field degree strengths of $l = 15$ and higher in the northern hemisphere suggest that this low-degree incoherence is primarily the result of actual structure.

5. Deep Compensation of Topography

5.1. Viscous Flow in a Compositionally Homogeneous Mantle

Isostatic models of topographic compensation are sometimes appropriate when a compensating mass anomaly is at shallow depths, such as cases in which topography is supported by relief on the crust-mantle interface. However, at depths sufficiently greater than the brittle-ductile transition it is more physically appropriate to consider dynamic flow rather than isostasy. Incompressible Newtonian flow in a viscous shell (i.e., most of the solid outer portion of a planet) can be determined analytically by propagating velocity and stress boundary conditions through the interior of the shell [*Hager and Clayton*, 1989]. A no-slip boundary condition is appropriate at the surface under the assumption that the upper crust does not participate in mantle flow. We prefer a free-slip boundary condition at the liquid core boundary, although other authors have also investigated flow with both free-slip and no-slip lower boundary conditions [e.g., *Michel et al.*, 2013]. The effect of a fixed lower boundary is to restrict flow and increase relaxation times. Our model predicts the distribution of flow that results from a mass sheet perturbation Ψ with units of kg m^{-2} at a radial position R_Ψ in the interior [see *James et al.*, 2013, appendices B and C]. A stepped viscosity structure can be incorporated into the model by combining the appropriate propagator matrices. The amplitude of the mass anomaly can be used along with solutions for the displacements on the upper and lower flow boundaries to forward model the surface equipotential and gravity. The degree-dependent admittance spectrum can then be found by dividing surface gravity by the amplitude of the perturbation to the upper boundary. The reference viscosity that we chose for our model affects only the velocity solutions and does not change the interface displacements. Admittance solutions are therefore dependent only on the relative changes in viscosity with depth. The viscosity profiles used in our models are given in Table 1.

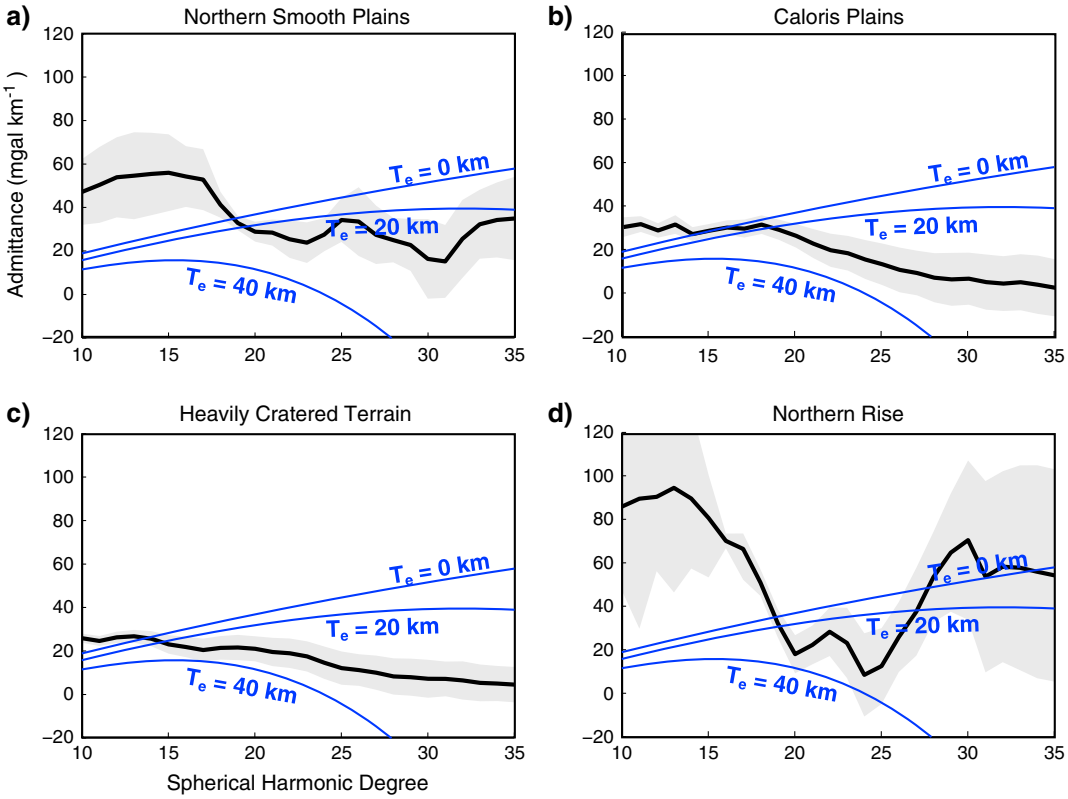

Figure 6. Observed admittance values (black) with error ranges (gray shading) and theoretical admittance values for bottom-loaded elastic shells having the indicated values of shell thickness T_e (blue).

The $l = 10$ admittance kernels in Figure 8 show the ratio of gravity to topography as a function of the loading depth $R - R_\Psi$, where R is the mean planetary radius, and the displacement kernel gives the amplitude of surface displacement scaled by Ψ/ρ_c, where ρ_c is the crustal density. In order to match the $l = 10$ admittance at the northern rise, a dynamic loading depth of $R - R_\Psi = 300$ km would be required for an isoviscous profile. The existence of a high-viscosity lithosphere does not appreciably change the modeled admittance spectrum. The presence of a high-viscosity layer at the base of the mantle, in contrast, decreases the admittances markedly. For a viscosity more than a factor of 2 greater than that of the overlying mantle, a 100 mGal km^{-1} admittance at $l = 10$ cannot be reproduced. A deep high-viscosity layer effectively couples the driving load Ψ to the lower boundary rather than to the surface and allows the gravity from Ψ to counteract the gravity from topography. If the viscosity of the deep layer is decreased, on the other hand, admittances are increased slightly over the isoviscous case.

The range of admittance values and the imperfect correlation of gravity and topography over much of the surface (cf. Figure 2) indicate that the topography of Mercury cannot be compensated by a single mechanism; the observed gravity and topography can be better fit by assuming the existence of at least two superimposed compensation mechanisms [*Banerdt*, 1986; *Herrick and Phillips*, 1992; *James et al.*, 2013]. The dual inversion required to separate two mechanisms has two constraints associated with each spherical harmonic function: the model must reproduce the observed gravity, and the radial stress at the surface must counteract the weight of topography. There are also two unknowns for a given spherical

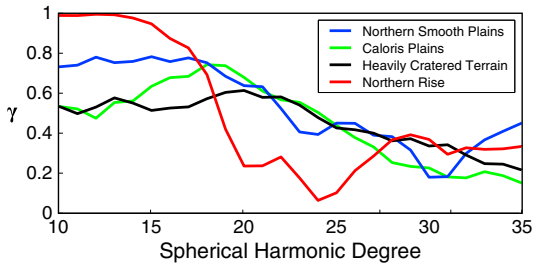

Figure 7. Spectral correlation of gravity and topography, calculated for each region via spatio-spectral localization.

Table 1. Profiles of Relative Viscosity[a]

Depths	Case 1	Case 2	Case 3
0–50 km	1	1	10
50–300 km	1	1	1
300–400 km	10	1	0.1

[a]Note that case 1 corresponds to high viscosity in the lower mantle, case 2 is isoviscous, and case 3 corresponds to a high-viscosity lithosphere and low viscosity in the lower mantle.

harmonic function: the finite-amplitude relief on the crust-mantle boundary [*Wieczorek and Phillips*, 1998] and the amplitude of a dynamic load. The dual inversion for crustal thickness and dynamic pressure is shown in Figure 9 for $\rho_c = 3200\,\mathrm{kg\,m^{-3}}$, a crust-mantle density contrast $\Delta\rho = 200\,\mathrm{kg\,m^{-3}}$, a mean crustal thickness of 40 km, and a mantle load depth of 350 km. Because deep compensation is associated with larger gravity anomalies than crustal isostasy, the inversion solution for dynamic pressure looks similar to Mercury's gravitational potential. In contrast, the crustal thickness variations contribute more to topographic relief than to the gravity field, so the crustal thickness solution looks similar to Mercury's topography.

5.2. Two-Layered Viscous Relaxation

Although the viscous flow models described above are instructive, the nature of viscous flow inside Mercury will be different if compositional layering exists above the 400-km deep boundary at the top of the liquid core, in that any flow across a boundary with an intrinsic density difference will produce an additional load driving flow (see Appendix D). We examine one particular scenario in which flow is driven by the relaxation of a perturbed FeS/silicate boundary (illustrated in Figure 10). In this "two-layered" viscous relaxation

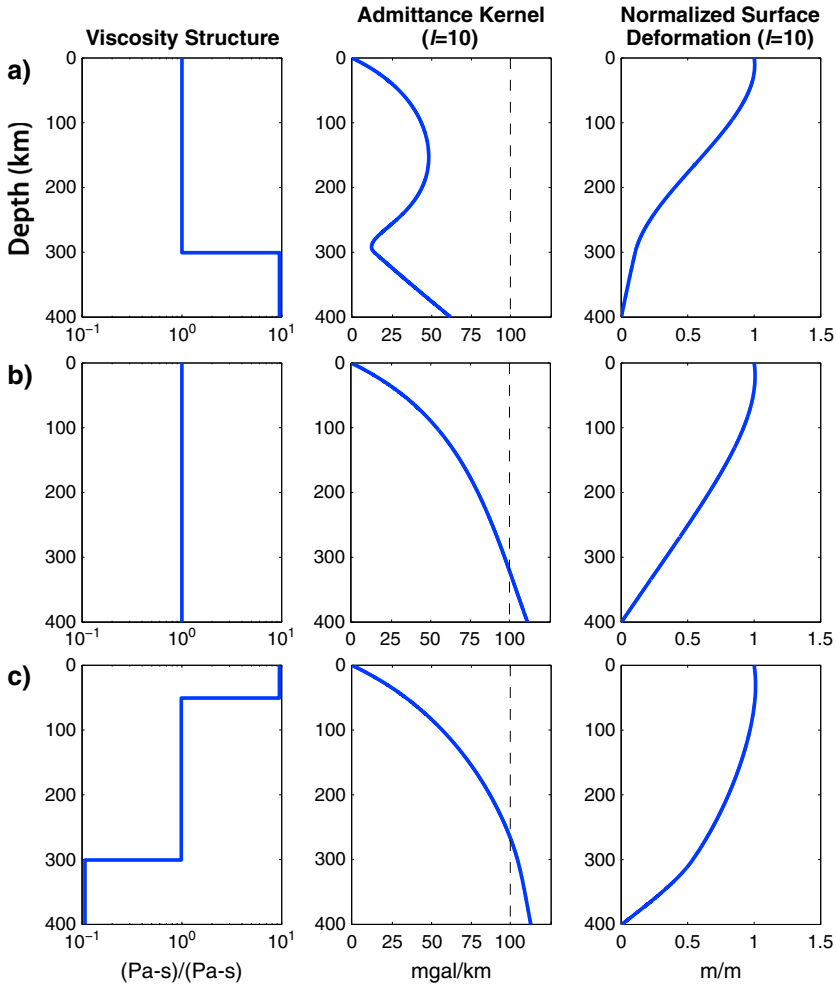

Figure 8. Admittance and surface displacement kernels for the three profiles of relative viscosity in Table 1.

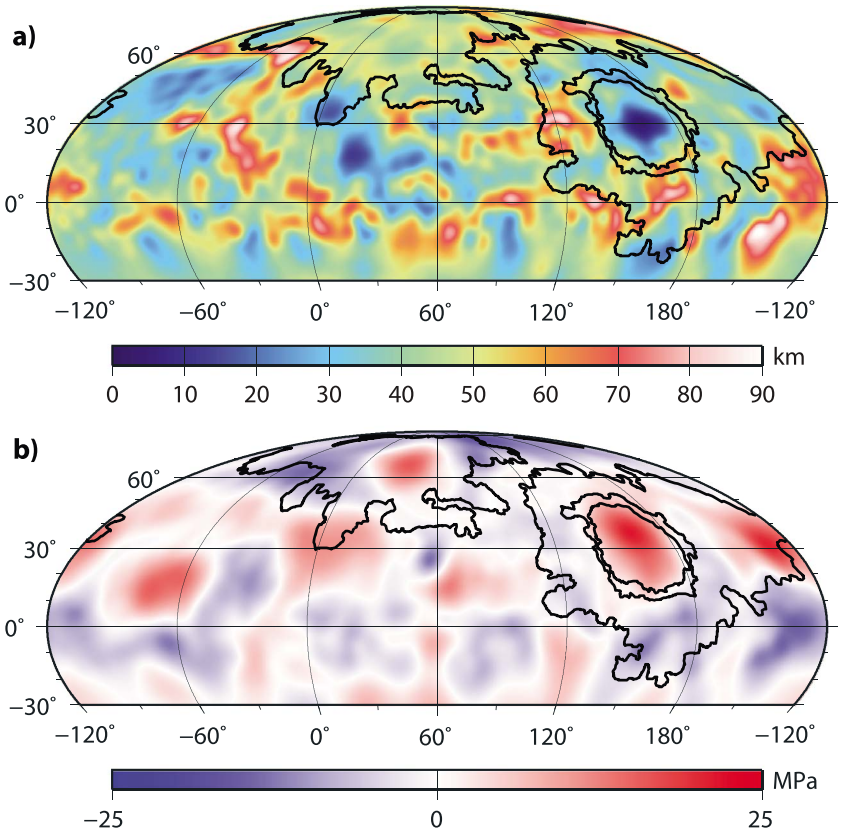

Figure 9. Two-layered model of topographic compensation: (a) crustal thickness and (b) surface pressure from dynamic flow (hot colors indicate upward pressure on the surface).

scenario, we invoke a 100-km thick layer of solid FeS below 300 km depth with a mantle/FeS density contrast of 1000 kg m^{-3} and an FeS/liquid core density contrast of 1300 kg m^{-3}. The thickness of the FeS layer is arbitrary but within the range of possible interior structure models [*Smith et al.*, 2012; *Hauck et al.*, 2013]. We also introduce a rigid lithosphere with a thickness of 150 km (within which viscosities are 100-fold larger than the viscosity of the underlying mantle), and we use crust and mantle densities of 3200 kg m^{-3} and 3400 kg m^{-3} [*Smith et al.*, 2012], respectively. The theory in Appendix D allows us to calculate the instantaneous radial velocities of the surface, the compositional layer, and the liquid core boundary. We used discrete time steps to calculate new interface amplitudes with these velocity solutions, and we used an adaptive time-stepping algorithm to propagate the solution forward in time.

Our semianalytical calculation begins with no surface topography and an FeS layer of laterally varying thickness. This thickness is prescribed by harmonic relief at the mantle-FeS interface, along with relief at the FeS-liquid core interface of opposite sign and proportional to the ratio of the respective density contrasts (i.e., the interior of the FeS layer is initially very close to a state of isostasy). The evolution of this configuration varies with the assumed viscosities, but the same basic chronology holds for most of parameter space: first, gravitational forces drive flow in the FeS layer away from thicker regions of the layer and toward thinner regions. As the thinnest parts of the FeS layer begin to swell, the overlying mantle buoyantly rises upward, and positive topography grows at the surface. Finally, at some point the viscous relaxation of surface topography overtakes the rate of uplift, and

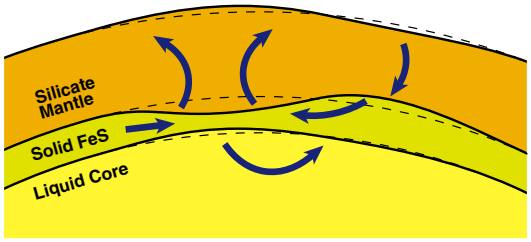

Figure 10. Schematic depiction of the layered relaxation problem in cross section.

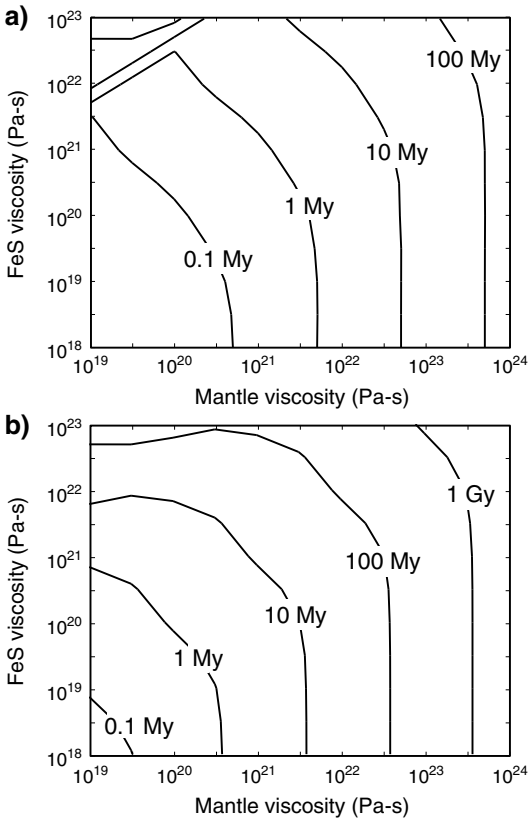

Figure 11. (a) Time of maximum topographic height and (b) timescale of topographic relaxation associated with two-layered perturbations of harmonic degree 8 (~1000 km half wavelength).

surface topography begins to relax toward zero amplitude. The characteristic timescale of topographic relaxation (defined here to be the time at which topography relaxes to one tenth of its maximum height) is typically an order of magnitude longer than the time of topographic uplift. Approximately 10–15 km of initial thinning of the FeS layer is required in order to create 1 km of surface topography. The admittance and displacement kernels associated with two-layered relaxation vary with time, but these kernels eventually converge to the values associated with chemically homogeneous models (cf. Figure 8) for which the loading depth $R - R_\Psi$ equals the depth of the mantle-FeS interface.

The duration of topographic uplift and the timescale of relaxation depend on the viscosities of the FeS layer and the silicate lower mantle (see Figure 11). If we assume that the viscosity of the FeS layer is less than that of the mantle, the timescales will not depend markedly on FeS viscosity. In this case, a relaxation time of 1 Gy would require a viscosity of more than 10^{23} Pa s in the lowermost mantle. It should be noted that this viscosity is still larger than the upper ends of the reference viscosity ranges respectively considered by *Michel et al.* [2013] (10^{19}–10^{21} Pa s) and *Tosi et al.* [2013] (10^{19}–10^{22} Pa s). As discussed in section 6.5, for the range of viscosity assumed by *Tosi et al.* [2013], topographic features at $l = 8$ would effectively relax on timescales of 0.05–30 My.

The timescales of topographic relaxation depend considerably on the aspect ratio of flow (i.e., the lateral length scale divided by the range of depths over which flow occurs). In analytical solutions of viscous relaxation in an infinite half-space, the longest wavelengths of surface relief relax most quickly [*Haskell*, 1936]; in contrast, the large aspect ratios associated with two-layered flow on a sphere with a thin mantle tend to prolong viscous relaxation at the longest wavelengths. Relative to relaxation at $l = 8$, perturbations at spherical harmonic degree 4 persist nearly 180% longer, and degree-12 perturbations relax 12% faster. For similar reasons, relaxation timescales vary with the depth of the mantle-FeS interface: relaxation is prolonged by nearly 140% if the interface is shallower by 50 km, and the timescale of relaxation is diminished by 20% if the interface is 50 km deeper in Mercury's interior. Viscous flow timescales will therefore have substantial uncertainties until the compositional profile of Mercury is better understood.

6. Discussion

6.1. High-Admittance Topography

The weight of topography on Mercury is likely supported by some combination of four compensation mechanisms: relief on the crust-mantle boundary, deep mass anomalies, lithospheric flexure, and lateral variations in density. If H^c is defined to be the portion of topography compensated by relief on the crust-mantle boundary ("crustally compensated topography"), we can define the power of this crustally compensated topography by the expression

$$S_l^{cc} = \sum_{m=-l}^{l} \left(H_{lm}^c\right)^2. \quad (1)$$

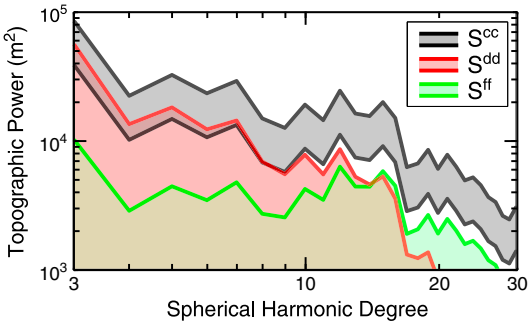

Figure 12. Expected ranges of topographic power resulting from crustal compensation (black), deep-seated dynamic flow (red), and flexural support (green), given the adopted parameter ranges (section 5.1).

Similarly, if H^d is the portion of topography compensated by deep mass anomalies ("deeply compensated topography") and H^f is the portion of topography supported by lithospheric flexure ("flexural topography"), then the respective power spectra S_l^{dd} and S_l^{ff} have similar forms.

We assess the relative importance of these three compensation mechanisms by calculating expected ranges of the power spectra S_l^{cc}, S_l^{dd}, and S_l^{ff} for adopted parameter ranges (Figure 12). The power spectrum when topography is compensated by crust-mantle boundary relief is assumed to be that of the topography multiplied by a factor between 0.5 and 1.1; here a factor of 1 corresponds to the case where topography is entirely supported by crustal thickness variations, and factors slightly higher than 1 indicate that crustally compensated topography is counteracted by another mechanism such as elastic stresses or deep compensation. The spectrum for dynamic loading is assumed to be equal to that for topography multiplied by a factor between 0.01 and 1.0, and the loading depth is taken to be 300 km. The power spectrum for flexurally supported topography is that for top loading with a magnitude less than or equal to the weight of topography and with λ = 1.5–5, where λ is in the ratio of top loading to bottom loading (see Appendix C) on a plate of thickness $20 < T_e < 100$ km.

Crustal compensation of topography is expected to be important for nearly all degrees less than $l = 30$, as demonstrated in Figure 12. However, the highest admittances shown in Figure 4 are too large to plausibly result from crustal thickness variations (some apparent compensation depths are greater than 100 km). Whereas flexural support and deep-seated compensation are associated with high-admittance values, flexure does not contribute substantially to topography at the lowest harmonic degrees for the parameter ranges given above. These considerations leave deep compensation as the most likely mechanism for support of the domical, high-admittance topographic swells.

6.2. Crustal Thickness

A crustal thickness map for Mercury was calculated by *Smith et al.* [2012] from gravity and topography data expanded to spherical harmonic degree and order 20, and *Mazarico et al.* [2014] calculated an updated map from data expanded to degree and order 50. These two models were "single-layer" inversions of gravity and topography, in that they fit the observed Bouguer gravity anomaly field by introducing finite-amplitude relief on the crust-mantle boundary [*Wieczorek and Phillips*, 1998]. The crustal thickness map presented in Figure 9a, in contrast, is a "dual inversion" of gravity and topography as described in section 5.1. Such a dual inversion introduces an extra assumption, namely, the mean depth of mantle mass anomalies, $R - R_\Psi$. The power of Mercury's crustal thickness (approximately proportional to S_l^{cc}, which is plotted in Figure 12) has a relatively shallow spectral slope that is approximately proportional to $l^{-0.8}$. This slope is in contrast to those for topography and crustal thickness on other terrestrial planetary bodies, which are generally more "red-shifted" (i.e., the spectra decrease more strongly with l [*Turcotte*, 1987; *Wieczorek*, 2007]). A nonnegativity constraint requires that the mean thickness be larger than 38 km. For a mantle that extends to 400 km depth, this lower bound means that the volume of crustal material is at least 11% of Mercury's silicate volume.

The quasi-linear rises on Mercury are associated with crustal thickening and are often superisostatic, with crustal roots deeper than is necessary to support the weight of topography. In many cases the crust underlying these rises is more than twice as thick as that of the surrounding terrain. The origin of the thickened crust is uncertain but may be the result of tectonic shortening or high degrees of mantle melting. The thickness of the crust under the quasi-linear rises is too large to be the result solely of Mercury's <8 km radial contraction in response to global cooling [*Byrne et al.*, 2014], so a tectonic origin of the rises may instead have been the result of surface tractions over convective downwellings. Alternatively, large volumes of melt may have resulted from the linear upwellings that are predicted by three-dimensional convection

Table 2. Ratios and Correlations of Topography Supported by Crustal Thickness Variations and Deeply Supported Topography

	Spherical Harmonic Degree	S_l^{dd}/S_l^{cc}	Correlation of H^c and H^d
NSP	10	1.74	−0.34
	15	0.62	0.09
Caloris plains	10	0.56	−0.55
	15	0.26	−0.39
HCT	10	0.32	−0.22
	15	0.19	−0.31

models [*King*, 2008]. Low-density residuum might be expected in sufficiently deep regions of extensive melt extraction [e.g., *Jordan*, 1978]. We would then expect to observe large admittances and good correlation of gravity and topography at the site of an extinct upwelling provided that the elastic lithosphere was not thick (i.e., $T_e < 100$ km for $l = 15$) at the time of residuum formation [cf. *James et al.*, 2013, Appendix C]. The absence of large admittances and good correlations at the quasi-linear rises (see Figure 2) indicates that (1) residuum is absent under the quasi-linear rises, (2) the gravitational and topographic effects of any residuum are obscured by unrelated crustal thickness variations, (3) residuum is characterized by a positive rather than a negative density anomaly (see further discussion of this possibility below), or (4) the elastic lithosphere was thick during and subsequent to the uplift of the rises. Lastly, some long-wavelength variations in crustal thickness may be remnants of ancient basin-scale impacts given the large number of large impacts expected during the period of heavy bombardment of the inner solar system. The time of formation of the quasi-linear rises may be constrained by measurements of crater floor tilts [cf. *Balcerski et al.*, 2012].

The thinnest crust in Figure 9a is found at the center of Caloris basin, an outcome consistent with excavation of much of the crust during the Caloris impact event. For a mean regional crustal thickness of 40 km, at least 1.0×10^7 km^3 of crustal material appears to have been ejected during the impact event. A central zone of thinned crust like the one in the Caloris basin is a common feature of lunar impact basins [*Zuber et al.*, 1994; *Neumann et al.*, 1996]. The crust surrounding the Caloris transient impact cavity may have collapsed inward during the early evolution of the basin [*Melosh et al.*, 2013], so the ~1000 km diameter of thinned crust can be considered a lower bound on the transient cavity diameter. The central region of thin crust is associated with buoyancy in the mantle, as is the rest of the CIP (Figure 9b). We also observe regions of thin crust and buoyant mantle centered at 15°N, 285°E and 35°N, 5°E, respectively, and it remains to be seen if these features are remnants of older basin-forming impact events.

6.3. Interpretation of Admittance and Coherence

We can quantitatively interpret the localized admittance and coherence spectra in terms of shallow and deep topographic compensation. If we represent the observed planetary shape as a superposition of crustally compensated topography H^c and deeply compensated topography H^d, the total topographic power can be expressed in terms of the power of H^c, the power of H^d, and the cross-power of H^c and H^d:

$$S_l^{HH} = \sum_m \left(H_{lm}^c + H_{lm}^d\right)^2 = S_l^{cc} + S_l^{dd} + 2S_l^{cd}. \tag{2}$$

Gravity power and cross-power spectra can be represented similarly if the crustal admittance spectrum Z^c and the admittances for deeply compensated topography Z^d are known (see Appendix C for theoretical admittance formulas):

$$S_l^{gg} = \sum_m \left(Z_l^c H_{lm}^c + Z_l^d H_{lm}^d\right)^2 = \left(Z_l^c\right)^2 S_l^{cc} + \left(Z_l^d\right)^2 S_l^{dd} + 2Z_l^c Z_l^d S_l^{cd} \tag{3}$$

and

$$S_l^{Hg} = \sum_m \left(H_{lm}^c + H_{lm}^d\right)\left(Z_l^c H_{lm}^c + Z_l^d H_{lm}^d\right) = Z_l^c S_l^{cc} + Z_l^d S_l^{dd} + \left(Z_l^c + Z_l^d\right) S_l^{cd}. \tag{4}$$

Equations (2)–(4) can, along with the observed admittance spectrum and gravity/topography correlations, be used to find the power and cross-power of H^c and H^d:

$$\frac{1}{S_l^{HH}} \begin{bmatrix} S_l^{cc} \\ S_l^{dd} \\ S_l^{cd} \end{bmatrix} = \begin{bmatrix} 1 & 1 & 2 \\ \left(Z_l^c\right)^2 & \left(Z_l^d\right)^2 & 2Z_l^c Z_l^d \\ Z_l^c & Z_l^d & Z_l^c + Z_l^d \end{bmatrix}^{-1}. \tag{5}$$

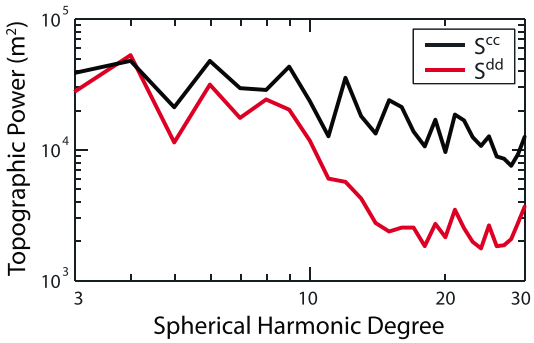

Figure 13. Power of crustal topography (black) and deeply compensated topography (red) resulting from a dual inversion of gravity and topography.

We can then calculate the ratio of topography power from deep sources over topography power from crustal variations, S_l^{dd}/S_l^{cc}, and the correlation of compensation sources, $S_l^{cd}/\left(S_l^{cc}S_l^{dd}\right)^{0.5}$ (see Table 2).

A majority of long-wavelength topography in the NSP is deeply supported. Ratios of S_l^{dd}/S_l^{cc} are lower but nonnegligible in the Caloris plains and the HCT, suggesting that deep mass anomalies are present and partially obscured by crustal thickness variations. The spherical functions H^c and H^d are relatively uncorrelated in the NSP, but they are negatively correlated in the Caloris plains and the HCT. In other words, thick crust is more likely to be associated with negative (downward) buoyancy in the mantle, and vice versa. The existence of positive mantle mass anomalies under the quasi-linear topographic rises is particularly intriguing.

6.4. What Are the Deep Mass Anomalies?

As shown in Figure 13, deeply compensated topography may be similar in amplitude to crustally compensated topography at low harmonic degrees. The power of deeply compensated topography drops considerably at degrees higher than $l = 13$, so dynamic flow (or at least its surface expression) exists mostly at Cartesian wavelengths larger than $2\pi R/\sqrt{l(l+1)} \approx 1100$ km. The large amplitudes of dynamic topography as well as the bias of dynamic topography toward long wavelengths validates, in retrospect, our assumption that the high-admittance topography results from deep mass anomalies rather than flexural support.

Although the deep mass anomalies represented by the load Ψ apparently exist on Mercury and produce substantial surface topography, we have not specified the origin of these anomalies. One possibility is perturbation of an interface between layers of different density. In the two-layered flow scenario explored in section 5.2, this excess mass comes from relief on the interface between the mantle and a solid FeS layer, and a depression of about 10 km on the interface (18 km of total thinning of the FeS layer) is required to produce 1 km of surface topography. We have not identified a likely cause of such a perturbation, but impact events and spatially variable additions to or losses from the solid FeS layer as a result of exchanges with the liquid core are possibilities.

Compositional layering in the silicate mantle is an alternative to the assumption of a solid FeS layer at the base of the mantle. Density contrasts within a silicate mantle are considerably smaller than the 1000 kg m^{-3} contrast between mantle and FeS, and relaxation timescales would therefore be greater; for example, flow driven by a density contrast of 250 kg m^{-3} would be associated with timescales greater by a factor of 4 because of the proportionally smaller restorative forces. An interior interface with a small density contrast would need to have proportionally larger amplitudes of relief in order to support a given amount of surface topography. In practice, however, such a calculation reaches the limits of applicability of our semianalytical model. The propagator formulation uses a sheet-mass approximation that is inappropriate when interface relief has large amplitude relative to adjacent layer thicknesses. Furthermore, the propagator formulation cannot predict the onset of nonlinear flow regimes that may exist in the presence of extreme aspect ratios for flow.

Potentially important factors in Mercury's evolution, which we did not model, are temporal variations in temperature and composition. Secular cooling of Mercury has led to a decrease in planetary radius accommodated by lobate scarps and other contractional landforms [*Solomon*, 1976], and the large volume of crustal material on Mercury (at least 11% of Mercury's silicate volume according to section 6.2) indicates extensive chemical depletion of the underlying mantle. The rigid lithosphere does not participate in viscous flow because of its high yield strength, and the increased aspect ratios of flow under a thickening

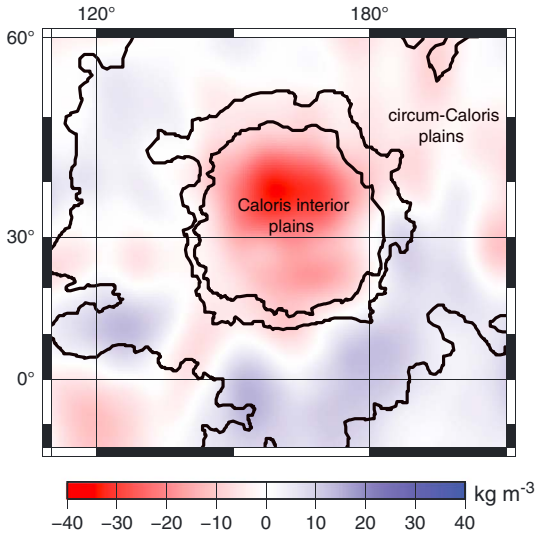

Figure 14. Mantle density anomaly in the vicinity of the Caloris plains units, outlined in black.

lithosphere will prolong two-layered relaxation. Thus, it may be possible to "freeze" topographic swells in place (although this word is a misnomer, all flow is in the solid state, and no phase transitions occur). Although our semianalytical two-layered flow calculation successfully incorporates a time-varying elastic lithosphere, models with time-varying viscosity profiles were numerically unstable, and future adaptations of our two-layered relaxation scheme (such as one involving layering within the mantle or time-varying viscosities) might be possible only with more flexible numerical calculations.

Another possible source of mass anomalies in Mercury's deep interior is lateral variation in density that can result either from thermal expansion/contraction or from compositional variations. For lateral temperature variations of up to $\Delta T = 300$°C, thermal density anomalies in the mantle may be expected to be approximately $\Delta\rho = \alpha\Delta T\rho_0 = 30\,\mathrm{kg\,m^{-3}}$, given a volumetric thermal expansion coefficient of $\alpha = 3\times10^{-5}$°C^{-1} and a reference density of $\rho_0 = 3300\,\mathrm{kg\,m^{-3}}$. Any thermal anomalies that remained after the cessation of convection and/or volcanism may have persisted for long periods of time before they conductively dissipated. To quantify this possibility, we approximated the thermal evolution of Mercury's interior with a one-dimensional heat diffusion calculation, with fixed temperature boundary conditions at the surface and at 400 km depth. For a thermal diffusivity of $\kappa = 10^{-6}\,\mathrm{m^2\,s^{-1}}$, a uniform temperature anomaly cools to one tenth of its initial anomaly at the center of the mantle after approximately 1.3 Gy. This figure should be considered an upper bound on the persistence time of temperature anomalies, since advective heat transport in the form of convection or volcanism would cool the mantle more rapidly.

Compositional variations may produce density variations comparable with those produced by thermal anomalies. For instance, if the lowermost mantle after early planetary differentiation could be approximated by an assemblage of 90% forsterite ($\rho = 3220\,\mathrm{kg\,m^{-3}}$) and 10% pyrope ($\rho = 3600\,\mathrm{kg\,m^{-3}}$), a chemically depleted residuum of pure forsterite would have a density $38\,\mathrm{kg\,m^{-3}}$ lower. *Jordan* [1978] similarly concluded that density variations due to differing degrees of extraction of partial melt might be about ±1% in the Earth. Of course, the assemblage described above is appropriate only in the garnet stability field, i.e., at pressures greater than 1.0–1.5 GPa for a range of compositions [*Ringwood and Green*, 1966] and depths greater than ~80–120 km in Mercury's mantle. Extraction of partial melt typically yields a residuum of lower density when iron is preferentially removed, but the abundance of iron at Mercury's surface and thus in the source region of Mercury's mantle-derived magmas is low [*Robinson and Taylor*, 2001]. Preferential melting of an aluminous phase can leave the residuum lower or higher in density, depending on the dominant aluminous phase, which varies with pressure and thus depth. Magma ocean models predict the presence of plagioclase feldspar and clinopyroxene among other minerals in the uppermost portions of the solidified products of a magma ocean on Mercury [cf. *Brown and Elkins-Tanton*, 2009, and references therein]. Plagioclase has a lower density (~$2700\,\mathrm{kg\,m^{-3}}$) than average mantle material, and preferential melting of plagioclase might therefore yield a higher-density residuum. However, density anomalies shallower than 150 km depth would appear largely as variations in crustal thickness rather than deep anomalies in our dual inversion solutions.

We can model the effect of density anomalies distributed through the mantle (as opposed to a mass sheet Ψ at a single depth) by integrating the flow solutions for a range of loading depths. This flow field can be incorporated into a dual inversion similar to the one shown in Figure 9. Low-mantle densities from such an inversion correlate well with the CIP (Figure 14), a result that could signify chemical depletion associated with the basin-forming impact event or with subsequent plains volcanism [*Watters et al.*, 2009].

6.5. Summary of Potential Origins for High-Admittance Topography

If the deep mass anomaly Ψ is interpreted to be relief on an interface between silicate mantle and an FeS layer, gravitational forces will drive that interface to relax toward an equipotential surface. We quantified the resulting flow patterns using a two-layered relaxation model (see section 5.2), and the relaxation timescales associated with a variety of mantle and FeS viscosities are shown in Figure 11. If the viscosity of FeS is lower than that of the mantle, then a viscosity of more than 10^{23} Pa s in the lowermost mantle is required in order to maintain surface topography over billions of years. Such a high viscosity contrasts with studies that predict long-lived mantle convection [e.g., *Tosi et al.*, 2013]. If the actual mantle viscosities are lower than 10^{23} Pa s, we may be confronted with a paradox: we observe long-lived, deeply supported topography on Mercury even though relaxation of such topography should have been relatively rapid. We have noted that larger aspect ratios of flow might markedly prolong relaxation (section 5.2), as might compositional stratification in the mantle (section 6.4), but other explanations for high-admittance topography should be carefully considered.

Flexurally supported topography would, in some cases, feature high admittances such as the ones observed at domical swells, but it is not clear how topography might have evolved into such a state. In one scenario, elastic stresses may have "locked in" high topography (uplifted by some other transient process) before it could have relaxed. A version of this scenario can be quantified with our two-layered relaxation formulation, which incorporates an elastic shell that can grow with time (see Appendix D). After topography grows in the presence of a thin elastic lithosphere, cooling of the surface might substantially thicken the elastic lithosphere and thereby lock in the high topography. However, a temporally evolving elastic lithosphere had very little effect on the final topography in this scenario (supporting $<1\%$ of the peak topography for a final lithosphere thickness of $T_e = 100$ km), so this effect is not likely a major contributor to the support of domical swells.

The existence of lunar mascons demonstrates that it is possible for planetary topography to evolve into a state of elastically supported superisostasy [*Melosh et al.*, 2013]. However, among Mercury's regions of high-admittance topography, only Caloris features a mantle anomaly that is centered on an identifiable impact basin. An anomaly in the vicinity of the Budh and Sobkou basins (~35°N, 225°E) may be an additional mass concentration [*Smith et al.*, 2012; *Mazarico et al.*, 2014]. Unlike the lunar mascons, however, the Caloris anomaly is not confined to the central region of crustal thinning. Therefore, if Mercury's high-admittance topography were supported by elastic stresses at present, it would likely have evolved into that state through a process different from the processes that led to the lunar mascons.

Mantle convection on Mercury may be possible at present if viscosities are sufficiently low [*Michel et al.*, 2013; *Tosi et al.*, 2013], and such convection can produce high-amplitude dynamic topography under some conditions, but mantle convection patterns need not be stationary for billions of years. Additionally, the length scales of thermally driven convection do not match the observed length scales of deeply compensated topography: convection cells in a 366 km thick mantle would have Cartesian wavelengths of 650–750 km, which correspond to spherical harmonic degrees 20–23 [*Michel et al.*, 2013], in contrast to the observed dropoff in the power of dynamic topography at degrees higher than approximately $l = 13$. It is more likely that mass anomalies in the mantle would be relatively static, such as those arising from the compositional or thermal anomalies described in section 6.4. These mass anomalies could have any number of causes, including impact processes, regional melting, and inefficient mixing since early in Mercury's history, but it is unclear whether such anomalies could have produced topographic uplift after the emplacement of the largest expanses of volcanic plains.

7. Conclusions

The large admittance values (Figures 4–6) and the good correlation of gravity and topography (Figure 7) associated with Mercury's northern rise and Budh-Sobkou rise at spherical harmonic degrees less than 15 point to the existence of topographic compensation at 300–400 km depth and/or flexural top loading. The large amplitudes of high-admittance topography as well as the tendency for such topography to be most pronounced at length scales greater than 1100 km favors contributions from deeply compensated topography over flexurally supported topography. Flexural support of long-wavelength topography cannot be decisively ruled out, but the flexural loading would need to be more substantially shifted to longer wavelengths than the topography in

order to be compatible with the data. Deep-seated mass deficits that compensate the domical topographic swells may result from either lateral variations in density or from viscous relaxation of relief on a compositional boundary, such as the interface between the mantle and a solid FeS layer postulated to overlie the liquid core.

Our two-layered flow model demonstrates a process by which topography may grow and be sustained over geological timescales. The duration of two-layered dynamic flow is only marginally sensitive to the viscosity of a possible FeS layer. A lower mantle viscosity in excess of 10^{23} Pa s is required in order to maintain $l = 8$ topography for billions of years, although the requisite viscosity may be lower if Mercury's silicate shell is compositionally stratified.

A dual inversion of gravity and topography produces a crustal thickness map, and this analysis places a lower bound of 38 km on the mean thickness. Quasi-linear rises are found to be associated with thickened crust, often with more than double the crustal thickness of the surrounding terrain. Crustal thickness in the heavily cratered terrain and intercrater plains is weakly correlated with positive mass anomalies in the mantle. If the topographic rises in the heavily cratered terrain formed via early extensive partial melting of the mantle, the residuum in the source regions would have to be higher in density than unmelted mantle. An analysis of regionally localized admittance and coherence reveals that deeply compensated topography accounts for most of the $l = 10$ topography in the northern smooth plains. Deep-seated mass anomalies elsewhere on the planet may be present but are largely obscured by crustal thickness variations.

Appendix A: Data and Uncertainty Quantification

The sine and cosine coefficients for a spherical harmonic expansion can be represented in a single vector **c**. The covariance matrix of **c** is $\mathbf{\Sigma} = \mathbf{Q}\mathbf{\Lambda}\mathbf{Q}^{-1}$, where **Q** is the matrix of covariance eigenvectors and $\mathbf{\Lambda}$ is the diagonal matrix of covariance eigenvalues. We want to generate a vector of random errors **x** associated with the spherical harmonic coefficients. The multivariate normal distribution $f_{\mathbf{x}}$ for a given error vector **x** of length k is

$$f_{\mathbf{x}} = \frac{1}{(2\pi)^{\frac{k}{2}}|\mathbf{\Sigma}|^{\frac{1}{2}}}\exp\left(-\frac{1}{2}\mathbf{x}^{\mathbf{T}}\mathbf{\Sigma}^{-1}\mathbf{x}\right). \tag{A1}$$

For the sake of simplicity, we define a vector **y** related to **x** through a linear transformation:

$$\mathbf{y} \equiv \mathbf{Q}^{\mathbf{T}}\mathbf{x}. \tag{A2}$$

We can then define the multivariate normal distribution of a vector **y** in terms of the eigenvalue matrix $\mathbf{\Lambda}$:

$$f_{\mathbf{y}} = \frac{1}{(2\pi)^{\frac{k}{2}}|\mathbf{\Lambda}|^{\frac{1}{2}}}\exp\left(-\frac{1}{2}\mathbf{y}^{\mathbf{T}}\mathbf{\Lambda}^{-1}\mathbf{y}\right). \tag{A3}$$

Since $\mathbf{\Lambda}$ is a diagonal matrix, we can further decompose the density function in terms of the covariance matrix eigenvalues λ_n and vector components y_n:

$$f_{\mathbf{y}} = \prod_{n=1}^{k} f_n \tag{A4}$$

where

$$f_n = (2\pi\lambda_n)^{-\frac{1}{2}}\exp\left(-\frac{y_n^2}{2\lambda_n}\right). \tag{A5}$$

The cumulative distribution function (CDF) for a single variable is

$$\Phi_n = \int_{-\infty}^{y_n} f_n \partial y_n = \frac{1}{2}\left[1 + \mathrm{erf}\left(\frac{y_n}{\sqrt{2\lambda_n}}\right)\right]. \tag{A6}$$

For a series of k random CDF values selected on the interval $\Phi_n \in (0, 1)$, the values of y_n needed to reproduce that CDF are

$$y_n = \sqrt{2\lambda_n}\,\mathrm{erf}^{-1}(2\Phi_n - 1). \tag{A7}$$

The vector **y** can then be transformed back into the original coordinates:

$$\mathbf{x} = \mathbf{Q}\mathbf{y}. \tag{A8}$$

This expression is a random realization of spherical harmonic error, and a noisy set of spherical harmonic functions can be calculated:

$$\mathbf{c}_{\text{noisy}} = \mathbf{c} + \mathbf{x}. \tag{A9}$$

Appendix B: Spherical Harmonics and Admittance/Correlation Spectra

Mercury's shape $H(\Omega)$ may be expressed as a weighted sum of spherical harmonic functions:

$$H(\Omega) = \sum_{l=0}^{\infty} \sum_{m=-l}^{l} H_{lm} Y_{lm}(\Omega), \tag{B1}$$

where Y_{lm} is the 4π-normalized spherical harmonic function at degree l and order m and where negative orders correspond to sine terms. The coefficients H_{lm} are called the spherical harmonic coefficients of H, and the orthogonality of the spherical harmonic basis functions allows these coefficients to be calculated via simple integration:

$$H_{lm} = \frac{1}{4\pi} \iint_{\Omega} H(\Omega) Y_{lm}(\Omega) \mathrm{d}\Omega. \tag{B2}$$

When data are not evenly spaced over the surface of a sphere, it is common practice to alternatively calculate spherical harmonic coefficients via a least squares inversion of equation (B1). The free-air gravity anomaly $g(\Omega)$ can be similarly decomposed into its spherical harmonic coefficients g_{lm}. The cross-power spectrum of H and g is defined as the degree-wise sum over the product of H_{lm} and g_{lm}:

$$S_l^{Hg} = \sum_{m=-l}^{l} H_{lm} g_{lm}. \tag{B3}$$

Similarly, the power spectra of H and g are, respectively,

$$S_l^{HH} = \sum_{m=-l}^{l} H_{lm}^2 \tag{B4}$$

and

$$S_l^{gg} = \sum_{m=-l}^{l} g_{lm}^2. \tag{B5}$$

The wavelength-dependent ratio of gravity to topography is called the admittance spectrum, Z_l. The observed admittance function can be expressed in terms of power and cross-power spectra:

$$Z_l = \frac{S_l^{Hg}}{S_l^{HH}}. \tag{B6}$$

Another useful quantity is the correlation of gravity and topography, γ_l:

$$\gamma_l = \frac{S_l^{Hg}}{\sqrt{S_l^{HH} S_l^{gg}}}. \tag{B7}$$

The compensation mechanisms supporting planetary topography often produce characteristic admittance and correlation spectra, and consequently, the comparison of theoretical spectra with observed spectra allows us to probe the interior of a planet.

Appendix C: Admittances for Elastic Loading

We are interested in determining the gravitational perturbations caused by flexural loading on an elastic shell and how those perturbations scale to the height of topography. Flexural loads can be exerted at the top of the elastic lithosphere, at the base of the elastic lithosphere, or by some combination of top and bottom loading.

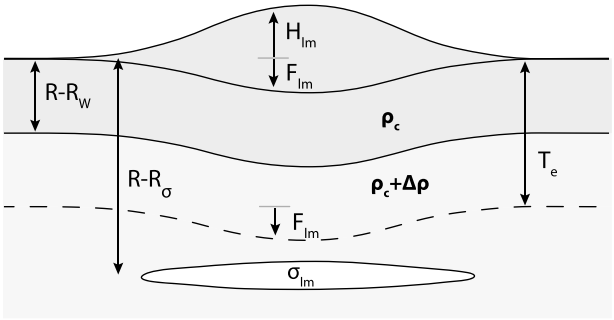

Figure C1. Schematic view of the flexural loading problem.

In order to quantify the loading state, we introduce a loading parameter λ that represents the ratio of top loading to bottom loading:

$$\lambda = -\left(\frac{R}{R_\sigma}\right)^2 \frac{\rho_c (H_{lm} - F_{lm})}{\sigma_{lm}}. \quad \text{(C1)}$$

where ρ_c is the density of the crust. The bottom load σ_{lm} at radius R_σ can then be expressed in terms of the planetary radius R, topography H, flexure F, and the loading ratio λ:

$$\sigma_{lm} = -\frac{\rho_c}{\lambda}\left(\frac{R}{R_\sigma}\right)^2 (H_{lm} - F_{lm}). \quad \text{(C2)}$$

Figure C1 illustrates the problem in cross section. The equation relating a load p to an elastic deflection F is given by *Turcotte et al.* [1981]:

$$\left(D\nabla^6 + 4D\nabla^4 + ET_eR^2\nabla^2 + 2ET_eR^2\right)F(\Omega) = R^4\left(\nabla^2 + 1 - \nu\right)p(\Omega). \quad \text{(C3)}$$

where E is Young's modulus, D is the flexural rigidity, and ν is Poisson's ratio in the elastic shell. In this formulation, toroidal flexure terms are neglected and laterally homogeneous material parameters are assumed. Solutions to equation (C3) can be written in terms of spherical harmonic coefficients:

$$\left[\frac{D}{R^4}\frac{-l^3(l+1)^3 + 4l^2(l+1)^2}{-l(l+1) + 1 - \nu} + \frac{ET_e}{R^2}\frac{-l(l+1) + 2}{-l(l+1) + 1 - \nu}\right]F_{lm} = p_{lm}. \quad \text{(C4)}$$

The first term in parentheses corresponds to bending stresses, and the second term corresponds to membrane stresses. We can alternatively write a flexure equation with a nondimensional flexure parameter e_l, which relates the amplitude of flexure to the uncompensated portion of topography:

$$e_l F_{lm} = -H_{lm}^{\text{uncompensated}} \quad \text{(C5)}$$

where e_l is

$$e_l = \frac{D}{\rho_c g_0 R^4}\frac{-l^3(l+1)^3 + 4l^2(l+1)^2}{-l(l+1) + 1 - \nu} + \frac{ET_e}{\rho_c g_0 R^2}\frac{-l(l+1) + 2}{-l(l+1) + 1 - \nu}. \quad \text{(C6)}$$

and where g_0 is the average surface gravitational acceleration. We substitute an Airy isostatic residual for the uncompensated topography in equation (C5):

$$(H_{lm} - N_{lm}) + \frac{\Delta\rho}{\rho_c}\left(\frac{R_W}{R}\right)^2 (F_{lm} - N'_{lm}) + \left(\frac{R_\sigma}{R}\right)^2 \sigma_{lm} = -e_l F_{lm}. \quad \text{(C7)}$$

where $\Delta\rho$ is the density contrast between crust and mantle and the radii R_W and R_σ correspond to the crust-mantle interface and the position of the bottom load, respectively. In order to account for self-gravitation, equation (C7) includes expressions for the local equipotential surfaces at the surface and the crust-mantle boundary, respectively:

$$N_{lm} = \frac{4\pi R^3}{M(2l+1)}\left[\rho_c H_{lm} + \left(\frac{R_W}{R}\right)^{l+2}\Delta\rho F_{lm} + \left(\frac{R_\sigma}{R}\right)^{l+2}\sigma_{lm}\right] \quad \text{(C8)}$$

and

$$N'_{lm} = \frac{4\pi R^3}{M(2l+1)}\left[\left(\frac{R_W}{R}\right)^{l}\rho_c H_{lm} + \frac{R_W}{R}\Delta\rho F_{lm} + \left(\frac{R_\sigma}{R_W}\right)^{l+2}\sigma_{lm}\right]. \quad \text{(C9)}$$

where M is the mass of Mercury. Equation (C7) can be rearranged to find the ratio of gravity to topography g_{lm}/H_{lm}, i.e., the admittance function for flexural loading on a self-gravitating sphere:

$$Z_l = \frac{g_{lm}}{H_{lm}} = 4\pi\rho_c G \frac{l+1}{2l+1}\left[1 - \left(\frac{R_W}{R}\right)^l \frac{(1-{}^1\Gamma_l)\chi_l + (R_\sigma/R_W)^l e_l + {}^1\beta_l}{(1-{}^2\Gamma_l)\chi_l + \lambda e_l + {}^2\beta_l}\right]. \tag{C10}$$

where G is the gravitational constant. This equation makes use of a parameter χ_l, two self-gravitational terms, and two terms associated with bottom loading:

$$\chi_l = \left(\frac{R_\sigma}{R_W}\right)^l + \lambda\frac{\Delta\rho}{\rho_c}\left(\frac{R_W}{R}\right)^2, \tag{C11}$$

$${}^1\Gamma_l = \frac{4\pi\rho_c R^3}{M(2l+1)}\left[1 + \frac{\Delta\rho}{\rho_c}\left(\frac{R_W}{R}\right)^{l+2}\right], \tag{C12}$$

$${}^2\Gamma_l = \frac{4\pi\rho_c R^3}{M(2l+1)}\left[\left(\frac{R_W}{R}\right)^l + \frac{\Delta\rho}{\rho_c}\frac{R_W}{R}\right], \tag{C13}$$

$${}^1\beta_l = \frac{\Delta\rho}{\rho_c}\left(\frac{R_W}{R}\right)^2\left[\left(\frac{R_\sigma}{R_W}\right)^l - 1\right], \tag{C14}$$

and

$${}^2\beta_l = 1 - \left(\frac{R_\sigma}{R_W}\right)^l. \tag{C15}$$

The bottom loading terms (C14) and (C15) arise when the bottom loading depth does not equal the depth of the crust-mantle interface.

Equation (C10) can be used for any ratio of top loading to bottom loading, but we can quantify the special cases of pure top and bottom loading. Bottom loading corresponds to a ratio $\lambda = 0$, and the resulting admittance spectrum is found by modifying equation (C10):

$$Z_l(\lambda = 0) = 4\pi\rho_c G\frac{l+1}{2l+1}\left[1 - \left(\frac{R_\sigma}{R}\right)^l \frac{1 - {}^1\Gamma_l + e_l + (R_W/R_\sigma)^l\,{}^1\beta_l}{1 - {}^2\Gamma_l(R_\sigma/R_W)^l}\right]. \tag{C16}$$

Similarly, we can calculate the admittance spectrum for a pure top-loading scenario (for which λ^{-1} approaches zero):

$$\lim_{\lambda\to\infty} Z_l = 4\pi\rho_c G\,\frac{l+1}{2l+1}\left[1 - \left(\frac{R_W}{R}\right)^l \frac{1 - {}^1\Gamma_l}{1 - {}^2\Gamma_l + \frac{\rho_c}{\Delta\rho}(R/R_W)^2 e_l}\right]. \tag{C17}$$

Considering the case $e_l = 0$ and $R_\sigma = R_W$, we find the admittance function for Airy isostasy corrected for self-gravitation:

$$Z_l\begin{pmatrix} e_l = 0 \\ R_\sigma = R_W \end{pmatrix} = 4\pi\rho_c G\,\frac{l+1}{2l+1}\left[1 - \left(\frac{R_W}{R}\right)^l \frac{1 - {}^1\Gamma_l}{1 - {}^2\Gamma_l}\right]. \tag{C18}$$

Appendix D: Two-Layered Flow

Dynamic flow in a viscous sphere can be calculated analytically by propagating velocity and stress boundary conditions through the interior [*Hager and Clayton*, 1989]. In addition to surface topography H and liquid core boundary relief C at radius R_C, we can imagine that there is a boundary B at radius R_B with an intrinsic density contrast $\Delta\rho_B$. The presence of such an interface alters the nature of steady state flow in Mercury's interior:

each increment of flow across B changes the radial load driving flow. Two-layered dynamic flow at a given spherical harmonic degree is governed by a system of four equations:

$$\begin{bmatrix} {}^*v_r(R) \\ {}^*v_\theta(R) \\ -{}^*\tau_{rr}(R) \\ -{}^*\tau_{r\theta}(R) \end{bmatrix} = \mathbf{P}_{RR_C} \begin{bmatrix} {}^*v_r(R_C) \\ {}^*v_\theta(R_C) \\ {}^*\tau_{rr}(R_C) \\ {}^*\tau_{r\theta}(R_C) \end{bmatrix} + \mathbf{P}_{RR_B} \begin{bmatrix} 0 \\ 0 \\ {}^*\tau_{rr}(R_B) \\ 0 \end{bmatrix}. \tag{D1}$$

Here velocity ($\mathbf{v}$) vector components and stress ($\boldsymbol{\tau}$) tensor elements are expressed according to the radial direction r and the poloidal lateral direction θ. The propagator matrices $\mathbf{P}_{RR_C}$ and $\mathbf{P}_{RR_B}$ contain information about the viscosity profile of Mercury (see Appendix B of *James et al.* [2013] for more information). Spherical harmonic coefficients have been dropped from each variable for the sake of concise notation. Additionally, all velocities and stresses are understood to be nondimensionalized as follows:

$$v = {}^*v \frac{g_0 \rho_m R^2}{\mu_0} \tag{D2}$$

and

$$\tau = {}^*\tau g_0 \rho_m R, \tag{D3}$$

where ρ_m is the mantle density and μ_0 is the reference viscosity. The radial stress at radius R is equal to the weight of displaced topography plus the pressure applied by elastic flexure:

$${}^*\tau_{rr}(R) = \frac{H - N}{R} + \frac{p}{\rho_m g_0 R}. \tag{D4}$$

The radial stresses at radii R_C and R_B can similarly be calculated:

$${}^*\tau_{rr}(R_C) = \frac{\Delta\rho_C g_C R_C}{\rho_m g_0 R^2}\left(C - N^C\right) \tag{D5}$$

and

$${}^*\tau_{rr}(R_B) = \frac{\Delta\rho_B g_B R_B}{\rho_m g_0 R^2}\left(B - N^B\right). \tag{D6}$$

The average gravitational accelerations at R_C and R_B are, respectively, g_C and g_B; in Mercury, these accelerations are approximately equal to g_0. The equipotential surfaces at radii R, R_C, and R_B are, respectively,

$$N = \frac{4\pi G R}{g_0(2l+1)}\left[\rho_m H + \Delta\rho_C C\left(\frac{R_C}{R}\right)^{l+2} + \Delta\rho_B B\left(\frac{R_B}{R}\right)^{l+2}\right], \tag{D7}$$

$$N^C = \frac{4\pi G R}{g_0(2l+1)}\left[\rho_m H\left(\frac{R_C}{R}\right)^{l-1} + \Delta\rho_C C + \Delta\rho_B B\left(\frac{R_B}{R}\right)^{l-1}\right], \tag{D8}$$

and

$$N^B = \frac{4\pi G R}{g_0(2l+1)}\left[\rho_m H\left(\frac{R_B}{R}\right)^{l-1} + \Delta\rho_C C\left(\frac{R_C}{R_B}\right)^{l+2} + \Delta\rho_B B\right]. \tag{D9}$$

Since the radial stresses are calculated in equations (D4)–(D6), we are left with six unknowns in four equations. In order to find solutions, we must first constrain two more parameters. We chose to do this by assuming no lateral velocities at the surface and no shear stresses at the liquid core boundary.

Radial velocity solutions are used to calculate radial displacements at each interface. Velocities at radii R and R_C are variables in equation (D1), and the radial velocity at R_B can be calculated with another propagator matrix:

$${}^*v_r(R_B) = \mathbf{P}^{11}_{R_B R_C} {}^*v_r(R_C) + \mathbf{P}^{12}_{R_B R_C} {}^*v_\theta(R_C) + \mathbf{P}^{13}_{R_B R_C} {}^*\tau_{rr}(R_C). \tag{D10}$$

We can then step the solution forward in time and modify the interface amplitudes:

$$\Delta H = {}^{*}v_r(R)\Delta t, \tag{D11}$$

$$\Delta C = {}^{*}v_r(R_C)\Delta t, \tag{D12}$$

and

$$\Delta B = {}^{*}v_r(R_B)\Delta t. \tag{D13}$$

We march forward in time using a dynamic time-stepping scheme: if the maximum interface change is less than 0.5%, then we increase Δt by a factor of 2, and if the maximum interface change is larger than 10%, we decrease Δt by a factor of 8. The incremental elastic response at a time step is a function of the elastic thickness [*Turcotte et al.*, 1981]

$$\Delta p = e_l \rho_c g_0 \Delta H \tag{D14}$$

where the elastic parameter e_l (defined in Appendix C) is continually updated to reflect the current elastic thickness.

Acknowledgments
We thank James Roberts and an anonymous reviewer for constructive reviews of an earlier version of this paper. We also thank Erwan Mazarico and Antonio Genova for providing us with early access to their gravity field solution. The MESSENGER project is supported by the NASA Discovery Program under contracts NASW-00002 to the Carnegie Institution of Washington and NAS5-97271 to The Johns Hopkins University Applied Physics Laboratory.

References

Anderson, J. D., G. Colombo, P. B. Esposito, E. L. Lau, and G. B. Trager (1987), The mass, gravity field, and ephemeris of Mercury, *Icarus*, *71*, 337–349.

Balcerski, J. A., S. A. Hauck II, P. Sun, C. Klimczak, P. K. Byrne, A. J. Dombard, O. S. Barnouin, M. T. Zuber, R. J. Phillips, and S. C. Solomon (2012), Tilted crater floors: Recording the history of Mercury's long-wavelength deformation, *Lunar Planet. Sci.*, *43*, Abstract 1850.

Banerdt, W. B. (1986), Support of long-wavelength loads on Venus and implications for internal structure, *J. Geophys. Res.*, *91*, 403–419.

Belleguic, V., P. Lognonné, and M. Wieczorek (2005), Constraints on the Martian lithosphere from gravity and topography data, *J. Geophys. Res.*, *110*, E11005, doi:10.1029/2005JE002437.

Brown, S. M., and L. T. Elkins-Tanton (2009), Compositions of Mercury's earliest crust from magma ocean models, *Earth Planet. Sci. Lett.*, *286*, 446–455, doi:10.1016/j.epsl.2009.07.010.

Byrne, P. K., C. Klimczak, D. A. Williams, D. M. Hurwitz, S. C. Solomon, J. W. Head, F. Preusker, and J. Oberst (2013), An assemblage of lava flow features on Mercury, *J. Geophys. Res. Planets*, *118*, 1303–1322, doi:10.1002/jgre.20052.

Byrne, P. K., C. Klimczak, A. M. C. Şengör, S. C. Solomon, T. R. Watters, and S. A. Hauck II (2014), Mercury's global contraction much greater than earlier estimates, *Nat. Geosci.*, *7*, 301–307, doi:10.1038/NGEO2097.

Cavanaugh, J. F., et al. (2007), The Mercury Laser Altimeter instrument for the MESSENGER mission, *Space Sci. Rev.*, *131*, 451–479, doi:10.1007/s11214-007-9273-4.

Charlier, B., T. L. Grove, and M. T. Zuber (2013), Phase equilibria of ultramafic compositions on Mercury and the origin of the compositional dichotomy, *Earth Planet. Sci. Lett.*, *363*, 50–60, doi:10.1016/j.epsl.2012.12.021.

Dahlen, F. A., and F. J. Simons (2008), Spectral estimation on a sphere in geophysics and cosmology, *Geophys. J. Int.*, *174*, 774–807, doi:10.1111/j.1365-246.

Denevi, B. W., et al. (2013), The distribution and origin of smooth plains on Mercury, *J. Geophys. Res. Planets*, *118*, 891–907, doi:10.1002/jgre.20075.

Evans, L. G., et al. (2012), Major-element abundances on the surface of Mercury: Results from the MESSENGER Gamma-Ray Spectrometer, *J. Geophys. Res.*, *117*, E00L07, doi:10.1029/2012JE004178.

Fassett, C. I., J. W. Head, D. T. Blewett, C. R. Chapman, J. L. Dickson, S. L. Murchie, S. C. Solomon, and T. R. Watters (2009), Caloris impact basin: Exterior geomorphology, stratigraphy, morphometry, radial sculpture, and smooth plains deposits, *Earth Planet. Sci. Lett.*, *285*, 297–308.

Forsyth, D. W. (1985), Subsurface loading and estimates of the flexural rigidity of continental lithosphere, *J. Geophys. Res.*, *90*, 12,623–12,632.

Hager, B. H., and R. W. Clayton (1989), Constraints on the structure of mantle convection using seismic observations, flow models, and the geoid, in *Mantle Convection: Plate Tectonics and Global Dynamics*, edited by R. W. Peltier, pp. 657–763, Gordon and Breach Science, New York.

Haskell, N. A. (1936), The motion of a viscous fluid under a surface load, II, *Physics*, *7*, 56–61.

Hauck, S. A., II et al. (2013), The curious case of Mercury's internal structure, *J. Geophys. Res. Planets*, *118*, 1204–1220, doi:10.1002/jgre.20091.

Hawkins, S. E., III et al. (2007), The Mercury Dual Imaging System on the MESSENGER spacecraft, *Space Sci. Rev.*, *131*, 247–338.

Head, J. W., C. R. Chapman, D. L. Domingue, S. E. Hawkins III, W. E. McClintock, S. L. Murchie, L. M. Prockter, M. S. Robinson, R. G. Strom, and T. R. Watters (2007), The geology of Mercury: The view prior to the MESSENGER mission, *Space Sci. Rev.*, *131*, 41–84, doi:10.1007/s11214-007-9263-6.

Head, J. W., et al. (2011), Flood volcanism in the northern high latitudes of Mercury revealed by MESSENGER, *Science*, *333*, 1853–1856, doi:10.1126/science.1211997.

Herrick, R. R., and R. J. Phillips (1992), Geological correlations with the interior density structure of Venus, *J. Geophys. Res.*, *97*, 16,017–16,034.

James, P. B., M. T. Zuber, and R. J. Phillips (2013), Crustal thickness and support of topography on Venus, *J. Geophys. Res. Planets*, *118*, 859–875, doi:10.1029/2012JE004237.

Jordan, T. H. (1978), Composition and development of the continental tectosphere, *Nature*, *274*, 544–548.

King, S. D. (2008), Pattern of lobate scarps on Mercury's surface reproduced by a model of mantle convection, *Nat. Geosci.*, *1*, 229–232, doi:10.1038/ngeo152.

Klimczak, C., T. R. Watters, C. M. Ernst, A. M. Freed, P. K. Byrne, S. C. Solomon, D. M. Blair, and J. W. Head (2012), Deformation associated with ghost craters and basins in volcanic smooth plains on Mercury: Strain analysis and implications for plains evolution, *J. Geophys. Res.*, *117*, E00L03, doi:10.1029/2012JE004100.

Leary, J. C., et al. (2007), The MESSENGER spacecraft, *Space Sci. Rev.*, *131*, 187–217.

Malavergne, V., M. J. Toplis, S. Berthet, and J. Jones (2010), Highly reducing conditions during core formation on Mercury: Implications for internal structure and the origin of a magnetic field, *Icarus*, *206*, 199–209, doi:10.1016/j.icarus.2009.09.001.

Margot, J.-L., S. J. Peale, R. F. Jurgens, M. A. Slade, and I. V. Holin (2007), Large longitude libration of Mercury reveals a molten core, *Science*, *316*, 710–714, doi:10.1126/science.1140514.

Margot, J.-L., S. J. Peale, S. C. Solomon, S. A. Hauck II, F. D. Ghigo, R. F. Jurgens, M. Yseboodt, J. D. Giorgini, S. Padovan, and D. B. Campbell (2012), Mercury's moment of inertia from spin and gravity data, *J. Geophys. Res.*, *117*, E00L09, doi:10.1029/2012JE004161.

Mazarico, E., A. Genova, S. Goossens, F. G. Lemoine, G. A. Neumann, M. T. Zuber, D. E. Smith, and S. C. Solomon (2014), The gravity field, orientation, and ephemeris of Mercury from MESSENGER observations after three years in orbit, *J. Geophys. Res. Planets*, *119*, 2417–2436, doi:10.1002/2014JE004675.

McAdams, J. V., R. W. Farquhar, A. H. Taylor, and B. G. Williams (2007), MESSENGER mission design and navigation, *Space Sci. Rev.*, *131*, 219–246.

McGovern, P. J., S. C. Solomon, D. E. Smith, M. T. Zuber, M. Simons, M. A. Wieczorek, R. J. Phillips, G. A. Neumann, O. Aharonson, and J. W. Head (2002), Localized gravity/topography admittance and correlation spectra on Mars: Implications for regional and global evolution, *J. Geophys. Res.*, *107*(E12), 5136, doi:10.1029/2002JE001854.

McKenzie, D. (1994), The relationship between topography and gravity on Earth and Venus, *Icarus*, *112*, 55–88.

McKenzie, D. (2003), Estimating T_e in the presence of internal loads, *J. Geophys. Res.*, *108*(B9), 2438, doi:10.1029/2002JB001766.

Melosh, H. J., et al. (2013), The origin of lunar mascon basins, *Science*, *340*, 1552–1555, doi:10.1126/science.1235768.

Michel, N. C., S. A. Hauck II, S. C. Solomon, R. J. Phillips, J. H. Roberts, and M. T. Zuber (2013), Thermal evolution of Mercury as constrained by MESSENGER observations, *J. Geophys. Res. Planets*, *118*, 1033–1044, doi:10.1002/jgre.20049.

Murchie, S. L., et al. (2008), Geology of the Caloris basin, Mercury: A view from MESSENGER, *Science*, *321*, 73–76, doi:10.1126/science.1159261.

Neumann, G. A., M. T. Zuber, D. E. Smith, and F. G. Lemoine (1996), The lunar crust: Global structure and signature of major basins, *J. Geophys. Res.*, *101*, 16,841–16,843.

Nittler, L. R., et al. (2011), The major-element composition of Mercury's surface from MESSENGER X-ray spectrometry, *Science*, *333*, 1847–1850, doi:10.1126/science.1211567.

Oberst, J., F. Preusker, R. J. Phillips, T. R. Watters, J. W. Head, M. T. Zuber, and S. C. Solomon (2010), The morphology of Mercury's Caloris basin, as seen in MESSENGER stereo topographic models, *Icarus*, *209*, 230–238, doi:10.1016/j.icarus.2010.03.009.

Peplowski, P. N., E. A. Rhodes, D. K. Hamara, D. J. Lawrence, L. G. Evans, L. R. Nittler, and S. C. Solomon (2012), Aluminum abundance on the surface of Mercury: Application of a new background-reduction technique for the analysis of gamma-ray spectroscopy data, *J. Geophys. Res.*, *117*, E00L10, doi:10.1029/2012JE004181.

Richards, M. A., and B. H. Hager (1984), Geoid anomalies in a dynamic Earth, *J. Geophys. Res.*, *89*, 5987–6002.

Ringwood, A. E., and D. H. Green (1966), An experimental investigation of the gabbro-eclogite transformation and some geophysical implications, *Tectonophysics*, *3*, 383–427.

Robinson, M. S., and G. J. Taylor (2001), Ferrous oxide in Mercury's crust and mantle, *Meteorit. Planet. Sci.*, *36*, 841–847.

Santo, A. G., et al. (2001), The MESSENGER mission to Mercury: Spacecraft and mission design, *Planet. Space Sci.*, *49*, 1481–1500.

Simons, M., S. C. Solomon, and B. H. Hager (1997), Localization of gravity and topography: Constraints on the tectonics and mantle dynamics of Venus, *Geophys. J. Int.*, *131*, 24–44.

Smith, D. E. (2014), GTMES_120V02_SHA, MESS-H-RSS_MLA-5-SDP-V1, NASA *Planetary Data System*. [Available at http://geo.pds.nasa.gov/messenger/mess-h-rss_mla-5-sdp-v1/messrs_1001/data/shadr/.]

Smith, D. E., et al. (2012), Gravity field and internal structure of Mercury from MESSENGER, *Science*, *335*, 214–217, doi:10.1126/science.1218809.

Solomon, S. C. (1976), Some aspects of core formation in Mercury, *Icarus*, *28*, 509–521.

Spudis, P. D., and J. E. Guest (1988), Stratigraphy and geologic history of Mercury, in *Mercury*, edited by F. Vilas, C. R. Chapman, and M. S. Matthews, pp. 118–164, Univ. of Arizona Press, Tucson.

Srinivasan, D. K., M. E. Perry, K. B. Fielhauer, D. E. Smith, and M. T. Zuber (2007), The radio frequency subsystem and radio science on the MESSENGER mission, *Space Sci. Rev.*, *131*, 557–571, doi:10.1007/s11214-007-9270-7.

Stockstill-Cahill, K. R., T. J. McCoy, L. R. Nittler, S. Z. Weider, and S. A. Hauck II (2012), Magnesium-rich crustal compositions on Mercury: Implications for magmatism from petrologic modeling, *J. Geophys. Res.*, *117*, E00L15, doi:10.1029/2012JE004140.

Tosi, N. M., M. Grott, A.-C. Plesa, and D. Breuer (2013), Thermochemical evolution of Mercury's interior, *J. Geophys. Res. Planets*, *118*, 2474–2487, doi:10.1002/jgre.20168.

Turcotte, D. L. (1987), A fractal interpretation of topography and geoid spectra on the Earth, Moon, Venus, and Mars, *J. Geophys. Res.*, *92*, E597–E601.

Turcotte, D. L., R. J. Willemann, W. F. Haxby, and J. Norberry (1981), Role of membrane stresses in the support of planetary topography, *J. Geophys. Res.*, *86*, 3951–3959.

Watters, W. A. F., M. T. Zuber, and B. H. Hager (2009), Thermal perturbations caused by large impacts and consequences for mantle convection, *J. Geophys. Res.*, *114*, E02001, doi:10.1029/2007JE002964.

Watts, A. B. (2001), *Isostasy and Flexure of the Lithosphere*, 458 pp., Cambridge Univ. Press, Cambridge, U. K.

Weider, S. Z., L. R. Nittler, R. D. Starr, T. J. McCoy, K. R. Stockstill-Cahill, P. K. Byrne, B. W. Denevi, J. W. Head, and S. C. Solomon (2012), Chemical heterogeneity on Mercury's surface revealed by the MESSENGER X-Ray Spectrometer, *J. Geophys. Res.*, *117*, E00L05, doi:10.1029/2012JE004153.

Wieczorek, M. A. (2007), Gravity and topography of the terrestrial planets, in *Planets and Moons*, *Treatise on Geophysics*, vol. 10, edited by T. Spohn, pp. 165–206, doi:10.1016/B978-044452748-6/00156-5.

Wieczorek, M. A., and R. J. Phillips (1997), The structure and compensation of the lunar highland crust, *J. Geophys. Res.*, *102*, 10,933–10,943.

Wieczorek, M. A., and R. J. Phillips (1998), Potential anomalies on a sphere: Applications to the thickness of the lunar crust, *J. Geophys. Res.*, *103*, 1715–1724.

Wieczorek, M. A., and F. J. Simons (2007), Minimum variance multitaper spectral estimation on the sphere, *J. Fourier Anal. Appl.*, *13*, 665–692, doi:10.1007/s00041-006-6904-1.

Wieczorek, M. A., and M. T. Zuber (2004), Thickness of the Martian crust: Improved constraints from geoid-to-topography ratios, *J. Geophys. Res.*, *109*, E01009, doi:10.1029/2003JE002153.

Wieczorek, M. A., et al. (2013), The crust of the Moon as seen by GRAIL, *Science*, *338*, 671–675, doi:10.1126/science.1231530.

Zuber, M. T., D. E. Smith, F. G. Lemoine, and G. A. Neumann (1994), The shape and internal structure of the Moon from the Clementine mission, *Science*, *266*, 1839–1843.

Zuber, M. T., et al. (2012), Topography of the northern hemisphere of Mercury from MESSENGER laser altimetry, *Science*, *335*, 217–220, doi:10.1126/science.1218805.